

# Polarimetry of a 22° halo

G. P. Können and J. Tinbergen

The linear polarization and intensity of a 22° halo has been measured simultaneously at seven wavelengths as a function of scattering angle. The polarization pattern is found to be dominated by a narrow peak centered at the halo angle. The amount of polarization in this peak is much higher than expected from Fresnel refraction alone. The observations are explained with a birefringence-diffraction halo polarization model. The effective diameter of the hexagonal face of the halo-generating crystals is found to be 41 and 54 μm for two separate scans. An independent single-wavelength parhelion observation indicates a stronger birefringence peak concentrated in an even smaller angular scattering range and a crystal diameter of 220 μm. Crystal sizes derived from the halo intensity distributions are found to be consistent with those obtained from polarization. The data demonstrate the power of halo polarimetry as a tool for detection and identification of birefringent crystals in terrestrial or extraterrestrial atmospheres.

## I. Introduction

The strong polarization of the inner limbs of refraction halos makes polarimetry a sensitive means for detecting low-intensity halos. This places the potentials of halo polarimetry for remote sensing of atmospheres next to that of other polarimetric methods, of which several have been applied successfully over course of time.<sup>1,2</sup> Inner-limb polarization is the result of birefringence of halo-generating crystals, which causes the halo to consist of two mutually shifted orthogonally polarized components.<sup>3,4</sup> In the open air, inner-limb polarization can be easily observed, particularly for parhelia. However, for a better understanding of halo polarization, clearly more quantitative observations are required, and such measurements have not yet been reported.

To fill this observational gap, we constructed a portable polarimetric camera equipped with a color filter of narrow bandwidth. With that camera we collected a parhelion picture, but then our set of measurements was unexpectedly improved. This happened at La

Palma when we operated a 1-m telescope equipped with a multichannel polarimeter for an observing campaign directed toward polarimetric detection of ice crystals in the upper atmosphere of Venus.<sup>5,6</sup> During that daytime campaign, cirrus spoiled a few hours of our primary observations, but fortunately that same cirrus produced a very clear 22° terrestrial halo. We used the admirable computer control of the telescope to scan the halo, recording its polarization at seven wavelengths simultaneously, and also took a picture with the polarimetric camera. This paper presents an analysis of our current set of measurements, with emphasis on the La Palma halo.

The sequence of this paper is as follows. In Section 2 the physical background of halo polarization is discussed and our previous halo polarization model<sup>4</sup> is reformulated on a more general basis. Also, we added a simple diffraction model to it. In Section 3 we derive an analytical model halo polarization distribution to be used for curve fitting the data. In Section 4 the La Palma halo observations are presented and discussed. Section 5 presents the single-wavelength observations of the parhelion. In Section 6 we compare our observations with those of others and draw some conclusions about the applications of halo polarimetry.

## II. Theory of Halo Polarization

### A. General Arguments

One of us (G. P. Können) has published a theoretical analysis of the polarization of refraction halos.<sup>4</sup> The basic physical approach can still be applied, but for the interpretation of our measurements we need to refor-

G. P. Können is with the Royal Netherlands Meteorological Institute, P.O. Box 201, 3730 AE de Bilt, The Netherlands. J. Tinbergen is with Kapteyn Observatory, Mensingheweg 20, 9301 KA Roden, The Netherlands.

Received 20 November 1990.

0003-6935/91/243382-19\$05.00/0.

© 1991 Optical Society of America.

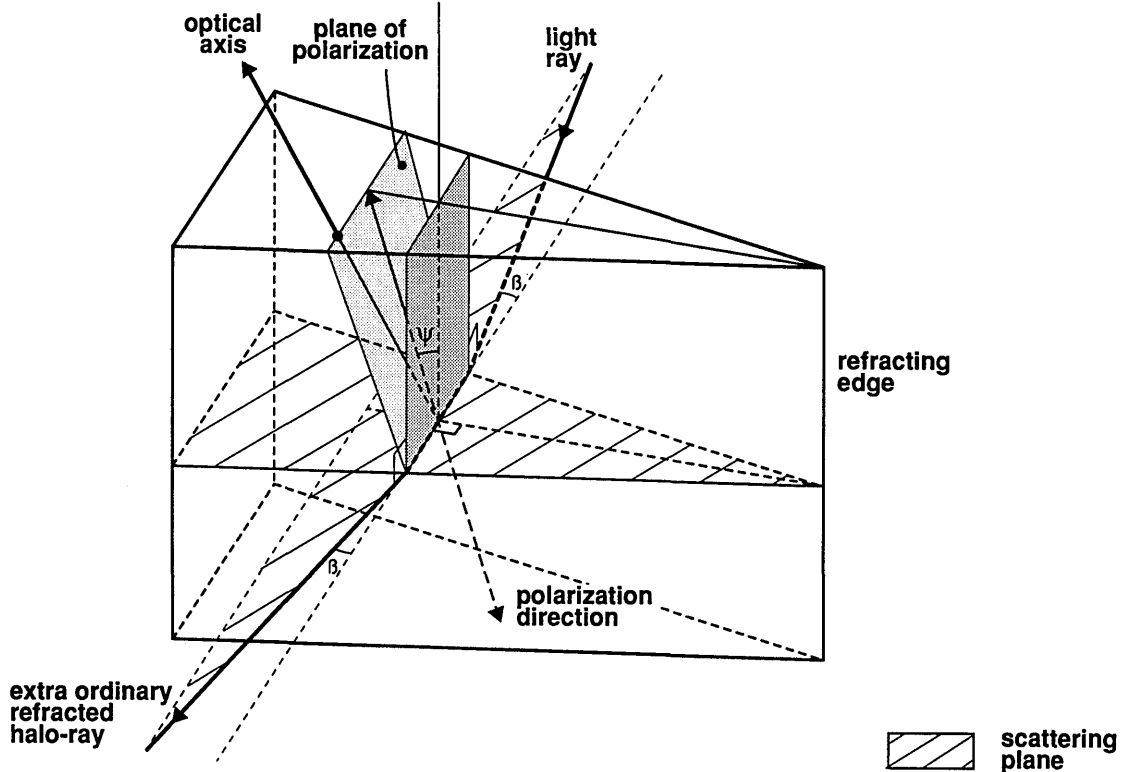


Fig. 1. Geometry of a crystal in the minimum deviation configuration. The refracting edge is perpendicular to the scattering plane. The plane of polarization of the extra-ordinary refracted ray is the plane formed by the light vector and the optical axis. The angle between this plane and the refracting edge is denoted by  $\psi$ . The plane of polarization of the ordinary refracted ray (not shown) is perpendicular to that of the extra-ordinary refracted ray. If the crystal is optically positive, the halo inner edge is formed by ordinary refracted rays, otherwise by the extra-ordinary refracted rays. There are two geometries contributing to halo edge scattering: the one depicted here and a second, with the crystal upside down. The Stokes parameter  $Q$  (reference in the scattering plane) is the same for both configurations; the signs of the linear Stokes parameters for extra-ordinary and ordinary refracted rays are opposite. The polarization of the halo inner edge is found by adding these contributions for the least refracted ray, leading to Eq. (1). For the  $22^\circ$  and  $46^\circ$  ice halos,  $\psi = 0$  and  $90^\circ$ , respectively.

mulate the model in more general terms. Before doing so, we give an outline of its underlying arguments.

First, we consider the intensity as a function of scattering angle for a refraction halo in the ray optics approximation, in which the birefringence of the crystals is neglected. The light source is taken to be a point source located at infinity. At one particular scattering angle, the intensity jumps from zero to a certain value. For any assumed distribution of crystal orientations this characteristic jump exists, and for all such distributions, except for  $\delta$  distributions, the jump is finite.<sup>4</sup> For light to be scattered at the angle of this discontinuity, a unique scattering geometry of the crystals is required. In the case of randomly oriented crystals—on which we shall focus from now on—this geometry is the minimum deviation configuration of the crystals. Hence, the light has to pass symmetrical-  
ly through the wedge consisting of the crystal faces at which refraction occurs.<sup>7</sup> The refracting edge, defined as the edge of this wedge, must be perpendicular to the scattering plane (see Fig. 1), and the scattering angle at which the jump occurs is called the halo angle.

The constraint on the orientation selects the subset

of crystals whose halo light is actually seen by the observer. In that subset, there is no random orientation at all. Near the halo angle, halo light is visible only from crystals that momentarily happen to have their refracting edge perpendicular to the scattering plane. Further away from the halo angle, there is a greater degree of freedom in the angle between the refracting edge and the scattering plane, so that a larger subset of the randomly oriented set of crystals may give rise to halo scattering from a certain point in the celestial sphere toward the observer. Still, the orientation constraint acts as a strong selection criterion so that the angle between the refracting edge and the scattering plane, projected on the celestial sphere, remains close to  $90^\circ$ .

Next we consider birefringence and assume the optical axis to be either parallel to the refracting edge or perpendicular to it. Then the halo consists of two orthogonally polarized components generated by ordinary and extra-ordinary refraction, respectively, each with its own refractive index and hence its own halo angle. For optically positive crystals (such as ice), the ordinary index of refraction is the lesser of the two.

We take this as an example. Then, at the inner side of the halo, only ordinary refraction is visible. The direction of polarization of ordinary refracted rays is always perpendicular to the plane formed by the light vector (inside the crystal) and the optical axis. However, as already pointed out, the halo-emitting crystals have their refracting edges perpendicular to the scattering plane. When the optical axis of the crystals is parallel with the refracting edge, the angle between this axis and the scattering plane is also  $90^\circ$ . Thus, the inner side of the halo, which, for optically positive crystals, is exclusively the result of ordinary refraction, is completely polarized and the direction of polarization is in the plane of scattering in this case. If the optical axis is perpendicular to the refracting edge, the same situation applies but the direction of polarization of the halo edge is perpendicular to the scattering plane (for positive crystals). We reemphasize that this strong polarization is a direct consequence of the high degree of orientation in the subset of crystals whose halo light is actually visible, which occurs even if the halo arises from a set of randomly oriented crystals.

If we look further away from the halo angle, there is a larger degree of freedom in the orientation of the refracting edge with respect to the scattering plane. This would result in a depolarization of both shifted halo components and a smaller mutual shift in scattering angle. In the model, these effects are neglected; the polarization of halos from birefringent crystals can then be calculated straightforwardly from the intensity distributions of the two polarized halo components.

The original model<sup>4</sup> used ray optics for the calculation of the polarization of halos. For interpretation of the present data, diffraction must also be considered. This can be done simply by convolving the Stokes vector  $S(\theta)$  of the halo, obtained in the ray optics approximation, with a diffraction function.<sup>8</sup> Below in this section, the resulting birefringence-diffraction model is formulated explicitly for randomly oriented uniaxial crystals with small birefringence and the optical axis either parallel to or perpendicular to the refracting crystal edge. However, for the more general case we make the following remarks:

(1) For halos caused by randomly oriented birefringent crystals, the polarization of the halo inner edge is always either in the plane of scattering or perpendicular to it. This holds for any orientation of the optical axis within the refraction wedge, as shown in remark (2) below. Hence, if the plane of reference of the Stokes parameters ( $Q, U$ ) is the scattering plane,  $U = 0$  and  $Q$  represents the polarized intensity  $I_{\parallel} - I_{\perp}$ , where the parallel and perpendicular signs refer to the scattering plane.

(2) If the optical axis is inclined to the refracting crystal edge, the polarization of the inner halo edge is generally not complete, even in the idealized situation of geometrical optics and a point-shaped light source. This polarization can be calculated using the fact that, inside a crystal, the polarization plane of the extraordinary refracted ray is the plane formed by the light vector and the optical axis, see Fig. 1. We consider

random orientation and hence the minimum deviation configuration. For the general case discussed here, the geometry of this configuration for extraordinary refracted light is slightly different from the isotropic case,<sup>9</sup> but, in practice, this difference is completely negligible. If we neglect the change in polarization at the entrance and exit faces of the crystal by refraction, the polarization direction of the inner edge and the degree of polarization of the birefringence peak can be easily calculated, the latter for the ray optics approximation. By definition, the first Stokes parameter equals intensity  $I$  and the second and third Stokes parameters  $Q$  and  $U$  are given by  $Q = PI \cos 2\phi$  and  $U = PI \sin 2\phi$ , respectively. Here  $P$  is the degree of polarization, which is unity for an extraordinary or an ordinary refracted ray, and  $\phi$  is the angle between the plane of polarization and the plane of reference of the Stokes vector. The plane of reference is chosen to be the scattering plane. In the minimum deviation configuration, it crosses the refracting edge at right angles, see Fig. 1. For determination of the halo polarization, one has to consider the polarization geometry of all the contributing crystal configurations. In the case of randomly oriented uniaxial crystals, there are always two of these: the one depicted in Fig. 1 and a second one with the crystal upside down. Let  $\psi$  be the angle between the refracting edge and the plane formed by the light vector and the optical axis. For the configuration shown in Fig. 1,  $\phi = \psi - 90^\circ$ ; for the second one,  $\phi = 90^\circ - \psi$ . Thus, the second Stokes parameter  $Q$  is the same for both configurations and equals  $-I \cos(2\psi)$  for extraordinary refraction (see Fig. 1). For ordinary refraction,  $\psi$  is larger by  $90^\circ$  and so the sign of  $Q$  is reversed. The polarization of the halo inner edge is found by adding  $Q$  from both configurations for the least refracted ray. Expressing the second Stokes parameter in degree of polarization  $P_x$ , this leads to

$$P_x \equiv Q/I = \text{sign}(n_e - n_o) \cos(2\psi). \quad (1)$$

Here  $\text{sign}(n_e - n_o)$  is the optical sign of the birefringent crystal. This factor takes into account whether the extraordinary or the ordinary refracted ray is the less refracted and hence responsible for scattering at the halo inner edge. For optically positive crystals such as ice,  $\text{sign}(n_e - n_o) = +1$ , ordinary refracted rays making up the inner halo edge.

Equation (1) nicely summarizes all the polarization possibilities of the inner edge of halos caused by randomly oriented uniaxial crystals. Since  $U = 0$  in that case [remark (1)], the degree of polarization  $P$  is given by  $|P_x| = |Q|/I$ , while the direction of polarization is given by the sign of  $Q$  or  $P_x$ . If  $P_x > 0$ , the polarization is in the plane of scattering, otherwise it is perpendicular to it. For the  $22^\circ$  ice halo,  $\psi = 0$  and thus  $P_x = +1$ . So, the plane of polarization of the halo inner edge is parallel to the scattering plane and its degree of polarization in geometrical optics and for a point-shaped light source is unity. For the  $46^\circ$  ice halo,  $\psi = 90^\circ$  and thus  $P_x = -1$ . Hence the polarization is again complete, but the direction of polarization is perpendicular

to the scattering plane. If a halo would emerge from a situation where  $\psi = 30^\circ$ , the degree of polarization of the halo inner edge is only 0.5; if  $\psi = 45^\circ$ , the polarization according to Eq. (1) is zero. Such decreased degrees of polarization of the birefringence peak may occur if, e.g., an ice halo is generated by a pair of pyramidal faces on either end of the crystal that are not adjacent to the same or to opposite prism faces. For some halos resulting from exotic crystals in other atmospheres, the same may happen. Finally, in the special case when the halo ray happens to be parallel to the optical axis, there is no split of the ray at all<sup>4</sup> and the halo behavior at the halo angle is the same as for isotropic crystals.

What remains to be proved is that  $U = 0$  for randomly oriented crystals. This is already evident from the geometry in Fig. 1, showing that the third Stokes parameter  $U$  of the two crystal configurations contributing to halo scattering is of opposite sign. This can also be proved considering the relations between  $\phi$  and  $\psi$ . We take the extraordinary ray as an example. Then, for the configuration shown in Fig. 1,  $\phi = \psi - 90^\circ$  and hence  $U = -I \sin 2\psi$ . If the crystal is upside down  $\phi = 90^\circ - \psi$  and so  $U = I \sin 2\psi$ . Hence, the contributions to  $U$  cancel out and thus  $U = 0$  for the halo. This proves the statement in remark (1).

(3) If preferential crystal orientation is present, the resulting halo usually has a noncircular shape. The inner boundary of this halo is again polarized and its polarization at a certain scattering azimuth can be found by considering the scattering geometry of the crystals responsible for scattering toward this boundary. As the refracting edge need not be perpendicular to the scattering plane in this case,  $U$  will in general be nonzero. Hence, the plane of polarization will be tilted with respect to the scattering plane. An illustrative example of this case is the parhelion, which appears at the same altitude as the Sun. Consequently, at the halo the scattering plane, being the great circle between halo and Sun, does not cross the celestial vertical at right angles. However, the parhelion results from ice crystals with the optical axis vertically oriented. As a result, the polarization of its inner edge is about horizontal, and this direction has a tilt with respect to the scattering plane.

(4) The actual polarization of the halo inner edge depends on the broadening of the birefringence peak by the solar disk and/or by diffraction. Since contributions to Stokes parameters can be added, a broadening leaves the direction of polarization unaltered. However, if the birefringence peak of the ray optical halo is narrow, the broadening results in a peak degree of polarization considerably less than that indicated by Eq. (1).

## B. Basic Formulas

Now we return to the case in which the optical axis and the refracting edge are either parallel ( $\psi = 0$  in Fig. 1) or perpendicular ( $\psi = 90^\circ$ ) and formulate the birefringence-diffraction model of halo polarization in the remainder of the section. This is done in the following

way. In this Subsection 2.B, we derive some general relationships between the intensity  $I(\theta)$  and the second Stokes parameter  $Q(\theta)$  of halos caused by birefringent crystals. In Subsection 2.C, the halo intensity distribution  $I(\theta)$  is specified as  $I_g(\theta)$ , being the one in geometrical optics and for a point-shaped light source at infinity. Using the technique in Subsection 2.B, the corresponding second Stokes parameter  $Q_g(\theta)$  of the halo is calculated. In Subsection 2.D, the broadening function  $g(\theta)$  is derived, which with  $I_g$  and  $Q_g$  must be convolved to take into account the broadening by diffraction and the solar disk smearing. The properties and interpretation of the resulting model are discussed in Section 3.

From now on we focus on random orientation and take the scattering plane as the plane of reference of the halo Stokes vector  $S(\theta)$ . Consequently, the third Stokes parameter  $U$  is zero, and so we deal with intensity and with the second Stokes parameter  $Q$  only.

Let  $f(\theta)$  be the intensity of a refraction halo generated by *isotropic* crystals,  $\theta$  the scattering angle, and  $f_1(\theta)$  and  $f_2(\theta)$  the intensities of the halo components with polarization in the plane of scattering and perpendicular to it, respectively. The ratio  $f_2/f_1$  is denoted by  $F$  and is determined by the Fresnel coefficients of refraction.  $F$  is a slowly decreasing function of  $\theta$ . At the halo scattering angle  $\theta_h$  and for geometrical optics, the relation  $F = \cos^4(\theta_h/2)$  holds. For a  $22^\circ$  halo, this latter expression yields  $F = 0.929$ . At  $\theta = 23^\circ$  and  $\theta = 26^\circ$ , its value is dropped by 0.006 and 0.015, respectively.

For *birefringent* crystals, the intensity distributions of the halo are denoted by  $I(\theta)$ ,  $I_1(\theta)$ , and  $I_2(\theta)$ . Introducing birefringence causes a splitting of the original halo into two components. The angular separation between them is denoted by  $\Delta\theta_h$ . We restrict ourselves to the case where the splitting takes place in the plane of scattering but note that, for a preferential orientation of the crystals, this need not be so.

For small birefringence the change of  $F$  with respect to the isotropic situation can be neglected.<sup>10</sup> Hence, under the above-mentioned assumptions we have

$$I_1(\theta) = \frac{1}{1+F} f(\theta + \frac{1}{2}\Delta\theta_h), \\ I_2(\theta) = \frac{F}{1+F} f(\theta - \frac{1}{2}\Delta\theta_h). \quad (2)$$

For ice, the optical axis coincides with the crystallographic  $C$  axis. For the  $22^\circ$  halo and the  $46^\circ$  halo,  $\Delta\theta_h$  is  $+0.11^\circ$  and  $-0.15^\circ$ , respectively.<sup>4,9</sup> Here, the sign of  $\Delta\theta_h$  is determined by Eq. (1), in which  $\psi = 0$  and  $\psi = 90^\circ$ , respectively. We assume the function  $f$  to be differentiable, expand  $f$  in Eqs. (2) in a Taylor series near  $\theta$ , and then calculate the halo intensity  $I$  from Eqs. (2):

$$I(\theta) \approx I_1(\theta) + I_2(\theta) \approx f(\theta) + \frac{1}{2}\Delta\theta_h \frac{1-F}{1+F} f'(\theta) \approx f(\theta). \quad (3)$$

The latter approximation can be applied since the term in front of  $f'(\theta)$  is very small. Replacing  $f$  by  $I$  in Eqs. (2), we find for the second Stokes parameter  $Q$  the expression:

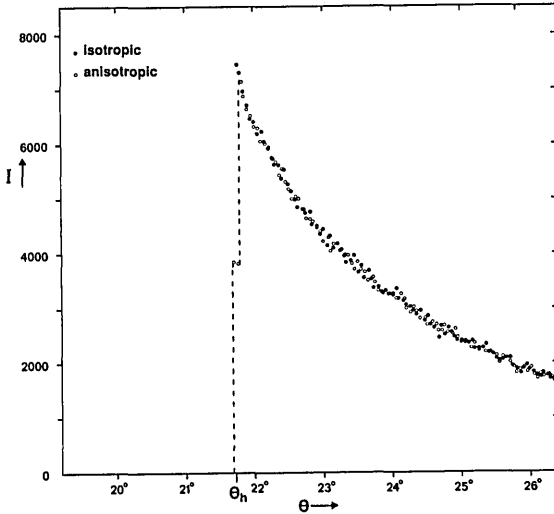


Fig. 2. Intensity of a 22° halo, simulated with a Monte Carlo program, for random orientation of ice crystals with equal-sized axes. The unit is counts/solid angle. The light source was a monochromatic point source at infinity. Results are shown for both isotropic and anisotropic crystals. The only difference is that for anisotropic crystals there is, near the halo angle  $\theta_h$ , a ledge of 0.1° width and of  $I = 3800$ . Within this ledge, only ordinary refraction contributes to halo scattering and hence the halo is completely polarized.

$$Q(\theta) \equiv I_1(\theta) - I_2(\theta) \equiv \frac{1-F}{1+F} I(\theta) + \frac{1}{2}\Delta\theta_h I'(\theta). \quad (4)$$

As mentioned above, the identity at the left-hand side of Eq. (4) is valid because the plane of reference of the Stokes vector  $S(\theta)$  is chosen to be the scattering plane. For the same reason, the third Stokes parameter of the halo  $U(\theta)$  is zero. Expressing Eq. (4) in degree of polarization  $P_x$ , we obtain

$$P_x(\theta) \equiv Q(\theta)/I(\theta) = \frac{1-F}{1+F} + \frac{1}{2}\Delta\theta_h I'(\theta)/I(\theta). \quad (5)$$

The first term in Eq. (5) is the classical value of the intrinsic degree of polarization of a refraction halo<sup>11</sup>; the second term is an additional one caused by birefringence.

The relation between  $I$  and  $f$ , Eq. (3), and the relation between  $Q$  and  $I$ , Eq. (4), can be tested with numerical simulations of halos. Figures 2 and 3 show the results of a Pattloch-Tränkle type Monte Carlo simulation<sup>12</sup> of the 22° ice crystal halo. The Monte Carlo program is from Tape<sup>13</sup> and was extended by us with a ray optical description of polarization and birefringence.<sup>10</sup> Figure 2 shows halo intensity simulations for isotropic and anisotropic crystals, in which only light rays resulting from two refractions have been counted (other contributions are negligible). As expected from Eq. (3), no significant difference between the anisotropic case and the isotropic case is apparent outside the range of the birefringence peak. Figure 3 shows the corresponding results for the second Stokes parameter  $Q$  of the halo. Also shown in Fig. 3 is  $Q$  for anisotropic crystals according to the current model, i.e., derived from isotropic simulation using Eq. (4).

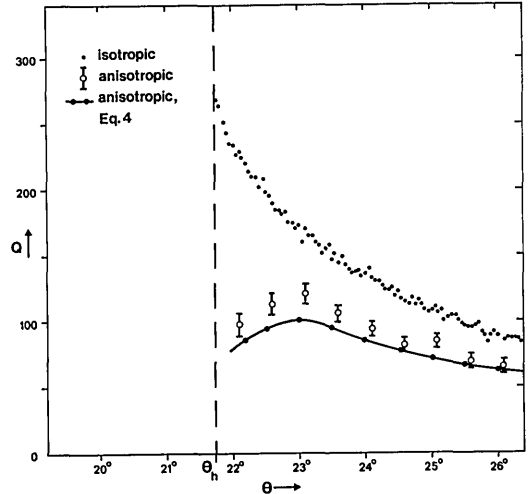


Fig. 3. Stokes parameter  $Q$  for the halo in Fig. 2. The plane of reference of the Stokes parameter is the scattering plane. The same units were used as in Fig. 2. Results shown are for isotropic crystals (solid circles) and for anisotropic crystals calculated from the isotropic data with Eq. (4) (curve). The open circles are the results of the Monte Carlo simulation for anisotropic crystals. The sharp birefringence peak near  $\theta_h$  is not shown here; it corresponds to the ledge in Fig. 2. Its width is 0.1° and its value is 3800 in the present units.

This curve compares well with the direct calculations at least up to a scattering angle of 30°, which includes the whole region of significance for a 22° ice crystal halo.<sup>14</sup>

### C. Halos in Geometrical Optics

We now consider the halo intensity function  $f_g(\theta)$  in geometrical optics for isotropic crystals and a point source of light at infinity. For randomly oriented crystals, as well as for all realistic cases of preferential crystal orientation, this function  $f_g(\theta)$  jumps<sup>4</sup> at the halo angle  $\theta_h$  from zero to a finite value  $f_g(\theta_h)$ ; for  $\theta > \theta_h$ ,  $f_g'(\theta) \leq 0$ . This behavior is apparent in Fig. 2. Hence, the halo intensity  $I_g(\theta)$  for birefringent crystals in geometrical optics and a point-shaped light source reaches its maximum ( $I_g$ )<sub>max</sub> after two jumps, see Eqs. (2). We define the halo angle  $\theta_h$  in birefringent crystals to be the mean of the halo angles for ordinary and extraordinary refracted rays so that the jumps take place at  $\theta = \theta_h - \frac{1}{2}|\Delta\theta_h|$  and  $\theta = \theta_h + \frac{1}{2}|\Delta\theta_h|$ , respectively. Hence  $(I_g)_{\text{max}} = I_g(\theta_h + \frac{1}{2}|\Delta\theta_h|)$ . Between these jumps,  $|Q_g| = I_g \cong \frac{1}{2}(I_g)_{\text{max}}$  and is, therefore, large with respect to the  $|Q_g|$ -value for larger values of  $\theta$ , at which Eqs. (4) and (5) still apply.

Now we assume  $|\Delta\theta_h|$  to be small compared to the broadening finite size of the solar disk and/or the diffraction pattern function, with which  $I_g$  and  $Q_g$  ultimately have to be convolved. Then we may in  $I_g$  neglect the birefringence by again using the approximation of Eq. (3):

$$I_g(\theta) \equiv I_{g1}(\theta) + I_{g2}(\theta) \cong f_g(\theta). \quad (6)$$

For  $Q_g$  we may apply Eq. (4), but near  $\theta = \theta_h$  the high  $|Q|$ -value has to be taken into account by a  $\delta$  function.

Put  $(I_g)_{\max} = f_g(\theta_h)$ ; for  $\Delta\theta_h > 0$  with Eqs. (2) and (6) this to

$$Q_g(\theta) = (I_g)_{\max} \frac{\Delta\theta_h}{1+F} \delta(\theta - \theta_h) + \frac{1-F}{1+F} I_g(\theta) + \frac{1}{2}\Delta\theta_h I_g'(\theta). \quad (7)$$

If  $\Delta\theta_h < 0$ , Eq. (7) can also be applied if the first term is multiplied by an additional factor  $F$ .

#### D. Diffraction

To get a more realistic model of the halo Stokes parameters, the ones derived from geometrical optics have to be convolved with a diffraction function with the solar disk and weighted with a particle size distribution. In this Subsection 2.D, we outline this procedure.

The diffraction pattern  $D(\theta)$  for a rectangular slit of width  $a$  producing its maximum intensity  $D_o$  at  $\theta = 0$  is given by<sup>15</sup>

$$D(\theta) = D_o \left( \frac{\sin x}{x} \right)^2, \quad (8)$$

where  $\theta$  is in the plane perpendicular to the slit and may be positive or negative. Parameter  $x$  is given by

$$x = \frac{\pi}{180^\circ} \frac{\pi a}{\lambda} \theta, \quad (9)$$

where  $\theta$  is in degrees. If the slit has a fixed length-to-width ratio,  $D_o$  is proportional to  $a^4/\lambda^2$  and slit width  $a$  for a crystal equals the width of the emerging light beam in the geometric approximation.

For a cloud of crystals, Eq. (8) has to be weighted with the crystal size distribution. If the size distribution is broad enough, this results in a function without oscillations. This is, for example, the case if a gamma distribution<sup>16</sup> is assumed. The width of the remaining diffraction peak at  $\theta = 0$  is related to the mean slit width, to be calculated from the mean surface area of the emerging beams and hence of the slit.<sup>15,16</sup> So, this effective mean is  $(a^2)^{1/2}$ . For a gamma distribution, the width of the diffraction peak for a given mean slit width turns out to be less than the primary diffraction peak of a single particle with a slit width equal to that mean.

Although it is known that crystal size distributions are peaked,<sup>17</sup> the size distributions may differ greatly from case to case. In our case, it is unknown. Instead of adopting an *ad hoc* size distribution, we chose for a simple model diffraction function, derived from Eq. (8) using the approximation

$$\left( \frac{\sin x}{x} \right)^2 \approx \frac{1}{1+x^2}, \quad (10)$$

where  $x$  is again given by Eq. (9) with  $a$  being replaced by  $a_{\text{eff}}$ , the effective slit width in the cloud of crystals. The function in relation (10) represents a model of the cross-sectional weighted diffraction function and consists of one diffraction peak without oscillations. If its integral over  $\theta$  is normalized to unity, this is the function with which the geometric halo functions  $I_g$  and  $Q_g$  have to be convolved to take diffraction and a broad crystal size spectrum into account. We call this function  $g(\theta)$ .

Figure 4 compares the adopted diffraction function

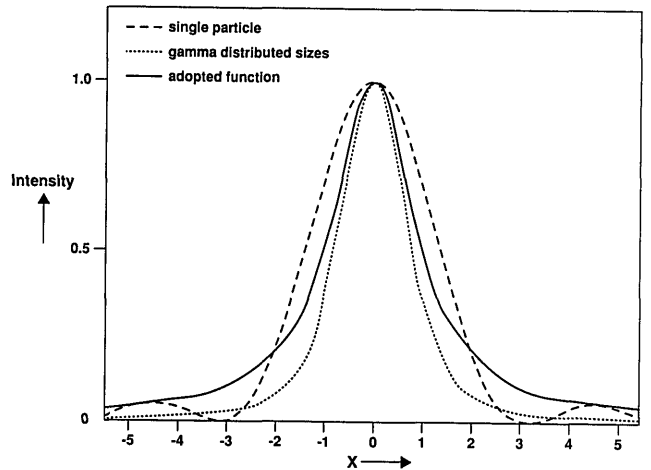


Fig. 4. Comparison of three diffraction functions.  $x = (\pi^2 a \theta) / (\lambda 180^\circ)$ , where  $a$  is the slit width and  $\theta$  is the deflection angle in degrees. The dashed curve is for a single particle. The dotted curve represents a gamma distributed set of slit widths; here  $a$  equals the effective mean slit width,  $(a^2)^{1/2}$ . The solid curve is the one adopted in this paper.

$g(\theta)$ , relation (10), with the diffraction function for a single particle, Eq. (8), and a function obtained by weighting Eq. (8) with a gamma distribution of sizes with  $n = 3$ . The latter size distribution approximately corresponds to the observed ones given in Ref. 17. As can be seen from Fig. 4,  $g(\theta)$  falls approximately between the others.

After normalization, the diffraction function  $g(\theta)$  becomes

$$g(\theta) = \frac{1/(\pi\theta_{1/2})}{1 + (\theta/\theta_{1/2})^2}, \quad (11)$$

where  $\theta_{1/2}$  is the angular separation between the diffraction maximum and its half-value point. This parameter relates to the effective slit width by means of

$$\theta_{1/2} = \frac{180^\circ}{\pi^2} \frac{\lambda}{a_{\text{eff}}}. \quad (12)$$

We note that, for Eq. (11) and for the single particle function  $\sin^2 x / x^2$  [Eq. (8)], the same normalizing constant  $1/\pi\theta_{1/2}$  applies.

The width of the Sun can be taken into account by an additional convolution of the halo functions with a function  $g_s(\theta)$ , which represents a disk:

$$g_s(\theta) = \frac{2}{\pi s^2} (s^2 - \theta^2)^{1/2}. \quad (13)$$

Here  $s$  is the semidiameter of the Sun. However, if the diffraction broadening is larger than  $s$ , we may still use Eq. (11), interpreting  $\theta_{1/2}(\text{tot})$  as caused by diffraction and by the solar disk. The diffraction part  $\theta_{1/2}$  can be simply calculated from  $\theta_{1/2}(\text{tot})$  using the Gaussian deconvolution rule<sup>14</sup>:

$$\theta_{1/2}^2(\text{tot}) = \theta_{1/2}^2 + \frac{1}{4}s^2. \quad (14)$$

The convolution integral, transforming the halo Stokes vector  $\mathbf{S}_g(\theta)$  in geometrical optics into the halo

Stokes vector  $\mathbf{S}_H(\theta)$  broadened by diffraction and by the solar disk, is given by

$$\mathbf{S}_H(\theta) = \int_0^\infty \mathbf{S}_g(x)g(x-\theta)dx. \quad (15)$$

### III. Model Halo Polarization Distribution and Its Interpretation

The convolution of the Stokes parameter of the geometrical optics halo with the function  $g(\theta)$  produces a model simulation of the polarization of a natural halo. We assume the observed signal to consist of a halo signal, superposed on a polarized background intensity. This background may result from several sources, among them scattering by air particles, by aerosols, and scattering by cloud particles by mechanisms other than halo scattering. We now change our notation a little,  $I_H(\theta)$  and  $Q_H(\theta)$  denote the intensity and second Stokes parameter of the halo after convolution with  $g(\theta)$ ;  $I_B$  and  $Q_B$  denote the corresponding parameters for the background. The total intensity and the total  $Q$  are denoted by  $I(\theta)$  and  $Q(\theta)$ , without subscripts. In this notation, the intrinsic degree of polarization of a halo (with  $U_H = 0$ ) is  $Q_H(\theta)/I_H(\theta)$  and may be denoted by  $P_H$ .

At a certain scattering angle, the convolved halo intensity  $I_H(\theta)$  reaches its maximum  $(I_H)_{\max}$ . In the following, we measure all the Stokes parameters,  $I_H$ ,  $Q_H$ ,  $Q_B$ , etc., relative to this maximum halo intensity  $(I_H)_{\max}$ . By definition, we put  $(I_H)_{\max}$  at unity. Since  $I_H(\theta)$  represents a convolution of a symmetrical function  $g(\theta)$  with a monotonically decreasing ray optics halo function  $I_g(\theta)$  (Fig. 2), this choice implies that the maximum intensity of the halo in geometrical optics  $(I_g)_{\max}$  is larger than unity.

Figure 3 indicates that  $Q_g$  is only a weak function of  $\theta$  in a large scattering angular range. We neglect this  $\theta$  dependence of  $Q_g$  by putting  $Q_g = C$  in Eq. (7) for  $\theta > \theta_h$ . Then, after convolution of Eq. (7) and  $g(\theta)$  by means of Eq. (15), we find the following model representation for  $Q(\theta)$ :

$$Q(\theta) = Q_H(\theta) + Q_B = \frac{A}{1 + ((\theta - \theta_h)/\theta_{1/2})^2} + C \left[ \frac{1}{2} + \frac{1}{\pi} \arctan \left( \frac{\theta - \theta_h}{\theta_{1/2}} \right) \right] + Q_B, \quad (16)$$

where background  $Q_B$  is assumed to be constant.

For the fit of the La Palma observations with Eq. (16), we also need a simple model representation of  $I(\theta) = I_H(\theta) + I_B(\theta)$ , to be used to transform the observed  $P_x$  into a value of  $Q$ . This representation can be a quite crude approximation, as the results of the polarization fit are not sensitive to the exact choice of  $I_H(\theta)$ . Since the La Palma measurements range no further than  $\theta = \theta_h + 3^\circ$ , for this approximation we can neglect the decrease of  $I_g(\theta)$  (Fig. 2) and represent  $I_g(\theta)$  by a step function. Then from Eqs. (11) and (15) we find that

$$I(\theta) = I_H(\theta) + I_B(\theta) = \frac{1}{2} + \frac{1}{\pi} \arctan \left( \frac{\theta - \theta_h}{\theta_{1/2}} \right) + I_B. \quad (17)$$

We note that, in general, the dependence of  $I_B$  on  $\theta$

cannot be neglected in model representations of the halo intensity, as is clear from Ref. 14 and from our measurements, but, for the purpose of transforming  $P_x$  to  $Q$ , we can keep  $I_B$  constant.

We also need an estimate for the ratio  $(I_g)_{\max}/(I_H)_{\max}$  to be used for the interpretation of  $A$ . This requires a somewhat better approximation for  $I_g(\theta)$  than the one leading to Eq. (17). We take for this an exponential function  $I_g(\theta) = (I_g)_{\max} \exp[-\alpha(\theta - \theta_h)]$  and approximate the convolving function by a constant that, according to Eq. (11), should be  $1/\pi\theta_{1/2}$ . Then,  $(I_H)_{\max}$  can be approximated by the mean value of  $I_g(\theta)$  in the interval  $\theta \in [\theta_h, \theta_h + \pi\theta_{1/2}]$ , yielding

$$(I_g)_{\max}/(I_H)_{\max} = \pi\alpha\theta_{1/2}/[1 - \exp(-\pi\alpha\theta_{1/2})]. \quad (18)$$

In this approximation,  $(I_H)_{\max}$  occurs at  $\theta = \theta_h + \frac{1}{2}\pi\theta_{1/2}$ . At that angle, we find from the exponential distribution and Eq. (18), that  $I_H(\theta)$  is almost equal to  $I_g(\theta)$ . This holds to within 10% if  $\alpha\theta_{1/2} < 0.5$ , which includes all cases of relevance.

The exponential approximation of the intensity distribution fits the simulated one surprisingly well. For the  $22^\circ$  Monte Carlo halo in Fig. 2,  $\alpha = 0.4 \text{ deg}^{-1}$ ; for the  $46^\circ$  halo from the same crystals,  $\alpha = 0.2 \text{ deg}^{-1}$ .

The model representation  $Q(\theta)$  is depicted in Fig. 5, which shows that the halo signal consists of the sum of a diffraction-broadened birefringence peak reaching its maximum value  $A$  at  $\theta = \theta_h$  and a smooth function that we may call the residual value of  $Q_H$ . The shape of the function describing this residual value is identical to that of the simple model representation of  $I_H(\theta)$  in Eq. (17).

The five free parameters in Eq. (16) contain the following information:

- $A$  determines the height of the sharp birefringence peak in  $Q_H$  measured relative to  $(I_H)_{\max}$ . The larger  $|A|$ , the more significant polarimetry is as a diagnostic for halos. Relaxing the condition that  $|\Delta\theta_h|$  is small with respect to the diffraction broadening of the peak for a moment, a general expression for  $A$  can be found from Eqs. (7), (11), and (15), where the  $\delta$  function in Eq. (7) is replaced by a rectangular function:

$$A = (I_g)_{\max} \frac{2/\pi}{1+F} \arctan \left( \frac{1/2\Delta\theta_h}{\theta_{1/2}} \right)$$

$$\approx \frac{(I_g)_{\max}}{\pi} \arctan \left( \frac{1/2\Delta\theta_h}{\theta_{1/2}} \right), \quad (19)$$

which is maximally  $\sim 0.5$ . For  $|1/2\Delta\theta_h| \lesssim \theta_{1/2}$ , it simplifies to

$$A \approx \frac{(I_g)_{\max}}{2\pi} \frac{\Delta\theta_h}{\theta_{1/2}}. \quad (20)$$

For the terrestrial  $22^\circ$  halo not broadened by diffraction [so  $\theta_{1/2} = 1/2 s$ ; see Eq. (14)],  $(I_g)_{\max} \approx (I_H)_{\max}$  [Eq. (18)] and the magnitude of  $A$  is 0.15. For large  $\theta_{1/2}$ , Eq. (18) and relation (20) indicate that  $A$  does not drop to zero, but reaches a limiting value of  $1/2\alpha\Delta\theta_h$ . For the  $22^\circ$  halo with  $\alpha = 0.4 \text{ deg}^{-1}$ , this limit is 0.02.

- $C$  is the residual polarization of the halo without

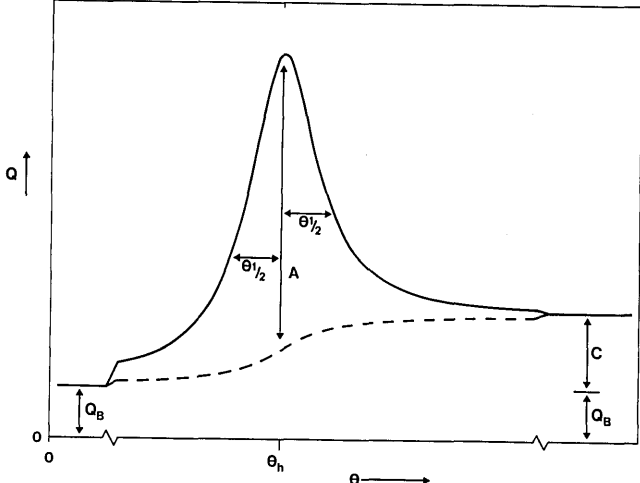


Fig. 5. Model representation for the second Stokes parameter  $Q$  of a halo. It consists of the sum of two terms: (1) a diffraction-broadened birefringence peak with amplitude  $A$  reaching its maximum at  $\theta = \theta_h$  and its half-maximum values at  $\theta = \theta_h \pm \theta_{1/2}$ ; (2) a smooth function with amplitude  $C$  represented by the dashed curve.  $Q_B$  is the background.

taking the birefringence peak into account. It is given by the last two terms in Eq. (7) divided by  $(I_H)_{\max}$ . We consider this expression at the scattering angle at which the halo intensity  $I_H$  reaches its maximum. At that angle,  $I_H \approx I_g$  and, therefore,

$$C = \frac{1 - F}{1 + F} + \frac{1}{2} \Delta \theta_h \frac{I'_g(\theta)}{I_g(\theta)}. \quad (21)$$

If birefringence is absent,  $C$  depends on the Fresnel coefficients alone and its value is 0.037 for the  $22^\circ$  halo. In the birefringent case,  $C - 0.037$  provides an estimate for the first derivative of  $I_g(\theta)$  and for its exponential parameter  $\alpha \equiv -I'_g/I_g$ .

- $A$  and  $C$  provide a value for the intrinsic degree of polarization of the halo in the absence of background intensity. This intrinsic polarization  $P_H$  peaks near  $\theta_h$  where the halo intensity  $I_H(\theta) \approx \frac{1}{2}(I_H)_{\max}$ . Hence, from Eq. (15) we have

$$(P_H)_{\max} \approx Q_H(\theta_h)/I_H(\theta_h) = 2A + C. \quad (22)$$

Outside the birefringence peak, say for  $\theta > \theta_h + 2\theta_{1/2}$  (see Fig. 4), the intrinsic halo polarization is of the order of residual polarization  $C$ . For still larger scattering angles,  $P_H$  starts to increase slowly. This is because  $Q_H(\theta)$  remains constant and  $I_H(\theta)$  decreases, see Figs. 2 and 3. This occurs outside the region of the La Palma observations.

- $Q_B$  is the background on which the halo signal is superposed. It may be caused by a number of effects, including single scattering by drops, aerosols, or by imperfectly shaped crystals, Rayleigh scattering, and multiple scattering in the cloud. The multiple scattering effects may cause a signal in the third Stokes parameter where no halo signal is present. We denote this component by  $U_B$ .

- $\theta_{1/2}$  with Eq. (12) provides a value for the effective slit width of the crystals  $a_{\text{eff}}$ . This slit width

represents the cross-sectional weighted width of the light beam emerging from the crystals. The determining factor of the slit width is the length of one of the crystal edges, hence one of the linear dimensions of the crystal. This length can be calculated from the scattering geometry of the crystals contributing to the birefringence peak. In the case of random orientation, this scattering geometry is the minimum deviation configuration with the refracting edge perpendicular to the scattering plane. For the  $22^\circ$  ice crystal halo, the slit width is determined by the length of the sides of the hexagon-shaped crystal face. The diameter  $d$  of this hexagon is found from

$$d = 2.65 a_{\text{eff}}. \quad (23)$$

For the  $46^\circ$  ice crystal halo, however, it depends on the aspect ratio of the crystal whether the slit width is limited by the sides of the hexagon or by crystal length  $l$ . For columns, the former situation holds so that  $a_{\text{eff}}$  provides redundant information about hexagon diameter  $d$  by means of  $d = 3.1 a_{\text{eff}}$ . For plates, however, the limiting edge length is crystal length  $l$ , a parameter that cannot be determined from the  $22^\circ$  halo. It can be calculated with  $l = 2.7 a_{\text{eff}}$ .

We note that an estimate for  $\theta_{1/2}$  and hence for the crystal size can also be obtained from the first derivative of  $I_H(\theta)$  at its inflection point near  $\theta_h$  (see, however, Lynch and Schwartz<sup>14</sup> for an alternative method). From the simple halo intensity distribution function given by Eq. (17) it follows immediately that

$$\frac{(I'_H)_{\max}}{(I_H)_{\max}} = \frac{1}{\pi \theta_{1/2}}. \quad (24)$$

Interestingly, the same formula can be applied for a less trivial intensity distribution  $I_H(\theta)$ , such as, for example, the one assuming an exponential behavior of the ray optical halo intensity  $I_g(\theta)$ . This is briefly outlined in Appendix A. On the other hand, it can be expected that the accuracy of  $\theta_{1/2}$  calculated from the slope of  $I_H(\theta)$  is often low compared with the one obtainable from  $Q$ , also because the observed intensity  $I(\theta)$  must be corrected for a background  $I_B(\theta)$ , which for circular halos must be guessed.

#### IV. La Palma Halo

##### A. Instruments

The observation took place at Observatorio del Roque de los Muchachos, La Palma, 22 June 1988. The altitude of the observatory is 2800 m and its geographic position is  $17^\circ 52'34''$  W,  $28^\circ 45'34''$  N. The instruments used were the Jacobus Kapteyn 1-m Cassegrain telescope and the Multi Purpose Fotometer (MPF).<sup>18</sup> The telescope was baffled and vignetted on the east side to prevent direct sunlight from reaching the mirror.<sup>19</sup> The telescope focal ratio is  $f/15$ , the focal plane diaphragm was 10 arcsec. During the halo scans, the solar elevation was  $70^\circ$  and the telescope was pointing westward at an elevation of around  $50^\circ$ . At that elevation, its absolute pointing accuracy is within 7 arcsec.

Table I. Status of the MPF During the Halo Scans<sup>a</sup>

Wavelength/Full Width at Half-Maximum Bandwidth (nm)	Number of Channels Used	Halo Angle	Error in $P \times 10^4$	$(P_x)_{\text{zero}} \times 10^4$	$(P_y)_{\text{zero}} \times 10^4$
402/10	1	22.56°	20	23 ± 2	-3 ± 2
441/10	2	22.32°	13	23 ± 3	6 ± 3
481/10	2	22.13°	16	26 ± 2	8 ± 4
542/10	1	21.91°	46	41 ± 6	1 ± 6
622/10	2	21.71°	10	6 ± 2	8 ± 2
712/10	1	21.55°	9	-7 ± 2	0 ± 2
791/10	2	21.43°	7	-3 ± 2	4 ± 2
850/30	1	21.35°	18	4 ± 3	-11 ± 3
590/33	Camera	21.79°	50	640 ± 100	215 ± 100

<sup>a</sup> The 22° halo angles were calculated using the indices of refraction of ice given by Hobbs,<sup>23</sup> which are valid with respect to vacuum and a temperature of -3°C. The halo angles given are the mean for ordinary and extraordinary refraction.  $P$  is the degree of polarization; its standard deviation is determined by photon statistics.  $(P_x)_{\text{zero}}$  and  $(P_y)_{\text{zero}}$  are the instrumental zero-point polarizations in the second and third Stokes parameters expressed in degrees of polarization. The plane of reference is the scattering plane. Data for the polarimetric camera are also included.

Details of the MPF are given elsewhere.<sup>18</sup> In this instrument, incoming polarized light is modulated at 100 Hz by a rotating half-wave plate. After passing an analyzing polarizer, the light is split into twelve beams by several beam splitters. Each beam subsequently passes a color filter and the photons are counted with photomultipliers. The integration time was 5.4 s for each point; after each integration there is a dead time of 5 s. The orientation of the coordinate system of the polarimeter with respect to the telescope frame was determined the next day at 17:00 UT (solar elevation 40°) by means of a measurement of the blue sky in the zenith. This method provided the angle between these frames to within an accuracy of 0.1°, confirmed by independent nighttime observations of standard stars.<sup>20,21</sup> The zero-point polarization of the system was determined at night by observing unpolarized first-magnitude stars.<sup>22</sup>

The MPF operated at eight different wavelengths; four wavelengths were observed twice. As the standard deviation of the polarization was determined by photon statistics, we averaged the results for channels with identical wavelengths  $\lambda$ . Table I summarizes the technical data. The photon statistics of the  $\lambda = 542$ -nm points turned out to be very poor with respect to the other channels. In the evaluation of the measurements the 542-nm data were not considered.

Additional information about the halo was obtained by means of a four-lens polarimetric camera of 125-mm focal length. This camera is a rebuilt commercial camera for passport photographs. Its purpose is to resolve fine-scale structures in polarization patterns such as the halo birefringence peak. It takes four pictures simultaneously on the same sheet film negative. Behind each lens is a polarizer, cut from the same sheet and with their orientations increasing in steps of 45°. The light then passes a filter with maximum transmission at 590-nm wavelength and 33-nm full width at half-maximum. The emulsion used was Kodak Tri-X. The relative transmissivity of the four lenses was determined from photographs of unpolarized objects such as the Sun and a white, backscattered bed sheet. The imaging characteristic of the four

lenses, determined from remote terrestrial objects, was found to be the same within 25 μm (0.01°). Therefore, digitized photos can be made to overlap by a simple translation procedure. The camera has a Sun finder; if the Sun is centered in that finder, the scattering angle in the images is known to within an accuracy of ~0.1°. This was calibrated with exposures of the horizon on a lake.

The halo negative was scanned with the Leiden Observatory Astroscan machine at a resolution of 50 × 50 μm (0.02° × 0.02°). After conversion from density to intensity, the pictures were made to overlap by the translation procedure and the Stokes parameters and degrees of polarization in each pixel were calculated. Subsequently, 5 × 5 pixel (0.11° × 0.11°) smoothing was applied. The standard deviation in the degree of polarization for one of these large pixels is of the order of  $5 \times 10^{-3}$ , enough to resolve fine-scale features. The uncertainty in the absolute value of the polarization may be two to three times higher, but this uncertainty only affects the background polarization on which the fine-scale features are superposed.

However, as the standard deviation of  $5 \times 10^{-3}$  is of the order of that of our poorest MPF channel, the degrees of polarization obtained did not contribute much to our polarization measurements of the La Palma halo. More important was the halo intensity distribution obtained by the camera, which was superior to the MPF scan by virtue of relatively uniform clouds. The second contribution of the camera was a picture of a parhelion taken on another occasion, which is discussed in Section 5.

### B. Halo

At La Palma, the cirrus cloud came in around 13:00 UT and overcast was reached around 13:30 UT. The halo became significantly bright around 14:15 UT, although there were local differences in halo brightness. Because of the strong northwesterly air flow, the clouds passed quite rapidly and from time to time the halo disappeared.

At 14:20 UT we decided to undertake attempts to scan the halo. The procedure was as follows. One of

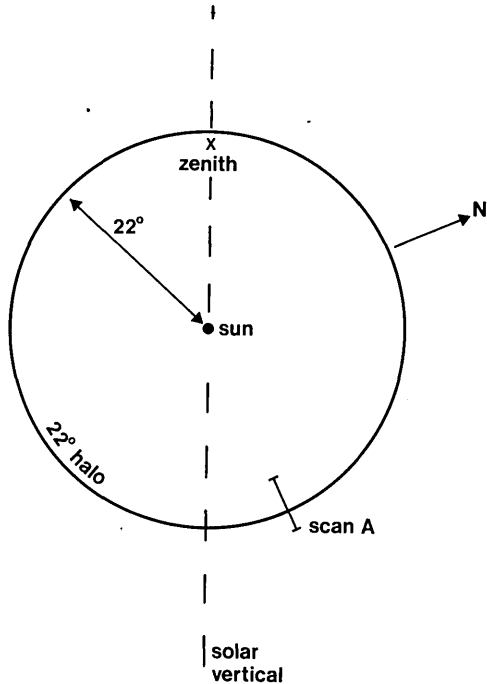


Fig. 6. Sketch of the situation during the La Palma halo scans. The solar elevation was  $\sim 70^\circ$  and the scans took place at an elevation of  $\sim 50^\circ$ . The track of scan A is indicated. Scan B followed the same track but was shorter. The direction of the celestial north is indicated. Polar projection.

us was in the telescope control room, the other in the dome watching the halo and the monitor displaying the data. The telescope declination was that of the Sun ( $23^\circ 25'$ ) and we scanned rapidly through the halo along this declination circle, west of the Sun. Hence, the halo scans took place along a track with a scattering azimuth of  $204^\circ$  with respect to the zenith. Figure 6 shows the circumstances of what we call scan A (see below); for the other scan the situation was similar. The right ascension scan rate was chosen to be 15 sec/s with respect to the fixed stars. Whenever the telescope right ascension passed an integer number of minutes, this was communicated via the intercom and the observation number at that moment was noted from the monitor screen. With these data it was possible to reconstruct the absolute time of these moments to within an accuracy of 1 s, and hence the absolute pointing of the telescope in the sky as known to within  $0.02^\circ$ . It took 1 min to scan through  $1^\circ$ , during which time about six integrations were collected. The integration time of 5.4 s corresponds to  $0.1^\circ$  smearing by telescope movement.

The first scan lasted from 14:22:17 to 14:26:26 UT and is called scan B. In that time interval 23 integrations were made, and the halo was quite stable. The scattering angular range covered was between  $18.7$  and  $22.4^\circ$ . This made the attempt only partly successful, since the halo angle was passed for only some of the wavelengths. A second scan, scanning the halo in the opposite direction, failed as the halo disappeared. However, 10 min later the halo reappeared and was

scanned from 14:39:40 to 14:46:26 UT, yielding 38 integrations in the scattering angular range of  $17.9$ – $24.0^\circ$ . During these measurements, which we call scan A, the halo was relatively bright and stable. During the twelfth integration (14:41:40 UT), a picture was obtained with the polarimetric camera (see Fig. 7).

After this successful measurement, a final attempt was undertaken to scan the halo in the reverse direction, starting at 14:47:27 UT, but soon the halo disappeared and subsequently the clouds also disappeared. At 14:55 UT the sky was again clear and we continued our observations of Venus.

The cirrus generating the La Palma halo can be identified in the NOAA-9 satellite picture taken at 16:15 UT. It was a fast-moving cirrus band associated with the subtropical jet stream. The cloud band passed all the Canary Islands, including the meteorological station at Tenerife. The vertical temperature sounding of 12:00 UT at that station can, therefore, also be considered as representative of our observing site. At a pressure level of 21.7 kPa, the sounding showed a maximum wind speed of 30 m/s from a northwest direction. In this jet, an inversion layer extended from 22.6 to 21.4 kPa with a minimum dew-point depression of  $10^\circ\text{C}$  at 22.6 kPa. Obviously the cirrus clouds were associated with that inversion, which was at a height of 11 km above sea level. The temperature of the humid layer was reported to be  $-53^\circ\text{C}$  at its bottom and  $-56^\circ\text{C}$  at its top.

Figures 8–10 show the results of scan A. The plane of reference of the Stokes vector ( $Q, U$ ) was rotated in such a way that  $Q$  is parallel to the scattering plane. The measurements for  $\lambda = 441$  and  $712$  nm are displayed; the results of the other five wavelengths are similar. The Stokes parameters are expressed in degree of polarization:  $P_x = Q/I$  and  $P_y = U/I$ . The solid curves in Fig. 8 are the result of a regression of the data with the model discussed in Section 3. Figure 11 is the halo intensity obtained from the densitometer scan of the halo picture, Fig. 7. Figure 12 shows  $P_x$  and the regression line for the incomplete scan B at  $\lambda = 712$  nm. For  $\lambda = 441$  nm, scan B did not extend to the maximum of  $P_x$ .

### C. Data Reduction

The MPF intensity measurements in Fig. 10 show much stronger fluctuations than can be expected from the internal standard deviations for the individual points. These fluctuations, which are absent in the photographic record of the intensity, Fig. 11, are correlated for different wavelengths and obviously result from the varying density of the moving clouds, see also the picture in Fig. 7. On the other hand, the scatter in the observed degrees of polarization  $P_x$  and  $P_y$  in Figs. 8 and 9 does agree with the internal standard deviations of the points. This means that the relative contribution of the halo to the total intensity remained constant during the intensity fluctuations. The direct observations of  $Q (=P_x I)$  obviously show the same fluctuations as the intensity points. Therefore, we prefer



Fig. 7. La Palma halo photographed during scan A. The field of view is  $15^\circ \times 19^\circ$ . The top of the picture points toward the zenith. The telescope scans took place near the right-hand edge of this picture. The clouds were moving to the left with an angular speed of  $9^\circ/\text{min}$ .

to use the observed  $P_x$  points for curve fitting with Eq. (16). These points are transformed to  $Q$  values by multiplication with the simple halo intensity function given by Eq. (17). This requires a value of the background intensity  $I_B$ , which is expressed relative to the maximum halo intensity  $(I_H)_{\max}$ . We note that the choice of  $I_B$  hardly influences the result for the regression constants  $\theta_h$  and  $\theta_{1/2}$  in Eq. (16) but does affect the

others. If the values of  $I_B$  given in Table II are increased by, e.g., 20%, the results of  $\theta_h$  and  $\theta_{1/2}$  only change by  $0.01^\circ$ , while  $A$ ,  $C$ , and  $Q_B$  increase by 15%, 10%, and 20%, respectively.

To reach consistency in the estimation of  $I_B$  for the different wavelengths, it was estimated as follows. For  $\lambda = 712 \text{ nm}$ ,  $I_B$  was determined directly from Fig. 10, yielding  $I_B = 1$  at the halo maximum with an

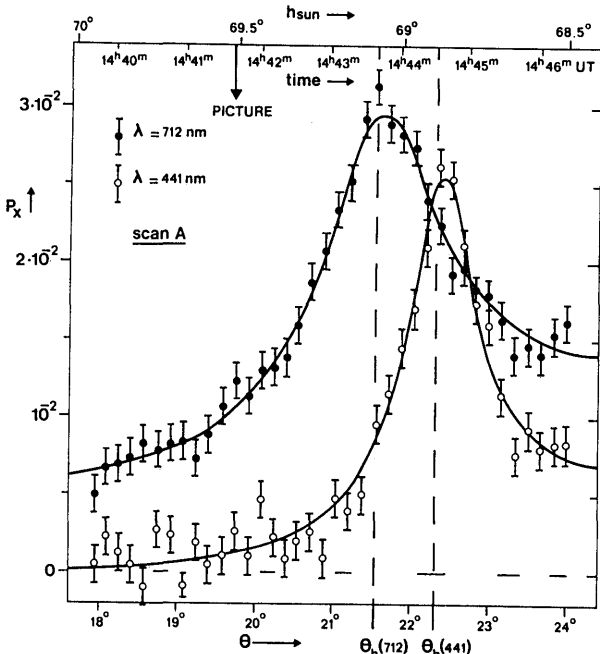


Fig. 8. Polarization of the La Palma halo for two wavelengths,  $\lambda = 712$  and  $441$  nm, observed during scan *A*.  $P_x = Q/I$  is the second Stokes parameter expressed in degree of polarization;  $\theta$  is the scattering angle. The plane of reference of the Stokes vector is the scattering plane.  $\theta_h$  is the halo angle for temperature  $T = -3^\circ\text{C}$  and averaged over the two directions of polarization. The solid curves are the best fit of the observations with the birefringence-diffraction model described in Section 3. The time and the solar elevation,  $h_{\text{sun}}$ , are indicated at the top of the figure. The moment the photograph (Fig. 7) was taken is indicated by an arrow. The halo was also recorded at five additional wavelengths; the results (not shown) are similar to those presented here.

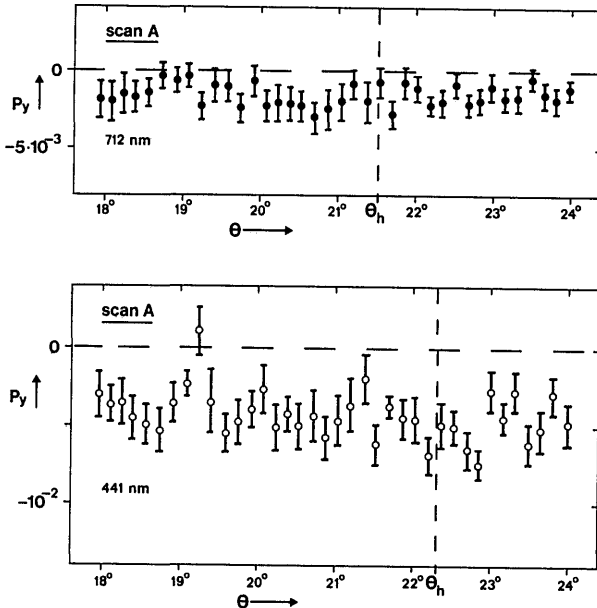


Fig. 9. Polarization of the La Palma halo of scan *A* for  $\lambda = 712$  and  $441$  nm.  $P_y = U/I$  is the third Stokes parameter expressed in degree of polarization;  $\theta$  is the scattering angle. The plane of reference of the Stokes vector is the scattering plane.  $\theta_h$  is the halo angle for  $-3^\circ\text{C}$  averaged over the two directions of polarization.

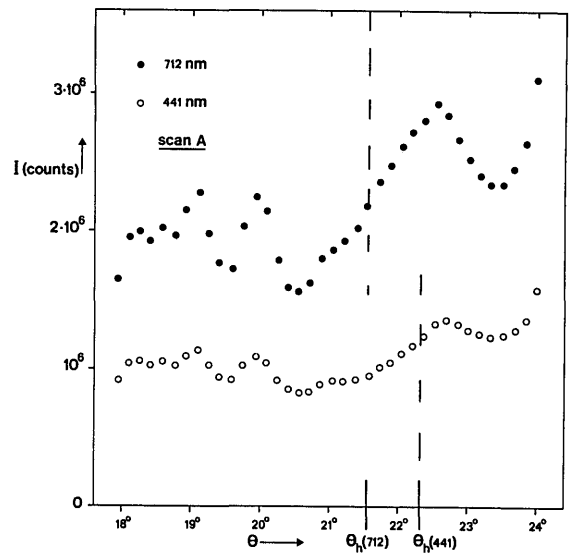


Fig. 10. Intensity  $I(\theta)$  of the La Palma halo of scan *A* in counts/point for  $\lambda = 712$  and  $441$  nm.  $\theta$  is the scattering angle,  $\theta_h$  is the halo angle for  $-3^\circ\text{C}$  averaged over the two directions of polarization. The standard deviation from photon statistics is of the order of  $10^3$ /point. The fluctuations in the measurements are determined by local density differences in the moving ice cloud.

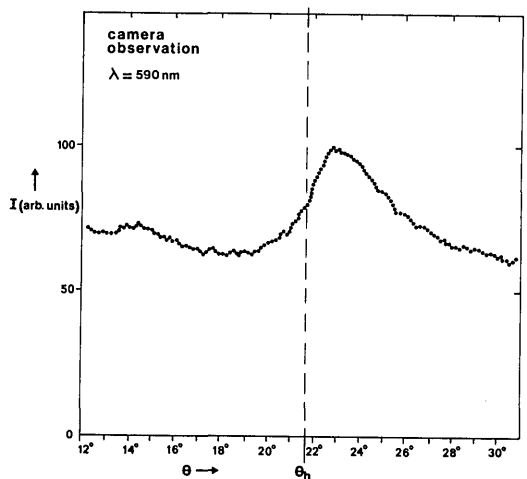


Fig. 11. Intensity of the La Palma halo during scan *A* as a function of scattering angle  $\theta$  obtained from the photograph in Fig. 7. The densitometer scan was taken through the uniform cloud in the middle of Fig. 7.  $\theta_h$  is the halo angle for the camera wavelength of  $590$  nm. The absolute value of the scattering angle contains an uncertainty of  $\sim 0.1^\circ$ .

estimated error of 20%. Then we determined the relative photon efficiency of the telescope/MPF combination for the various channels. This was done by using a calibration measurement on Vega, whose absolute spectral distribution is known.<sup>24,25</sup> The Vega elevation of  $70^\circ$  was the same as the solar elevation during the halo scans and the measurement took place the night following the halo observation. With this calibration, we determined the intensity per unit bandwidth  $d\lambda$  of the point at  $\theta = 18^\circ$  in the halo scan for the different wavelengths relative to that at  $\lambda = 712$  nm. This ratio is denoted here by  $R(\lambda)$ . Under the assumption that the halo is composed of randomly oriented ice crystals, the ratio of the intensities at two wavelengths is given by

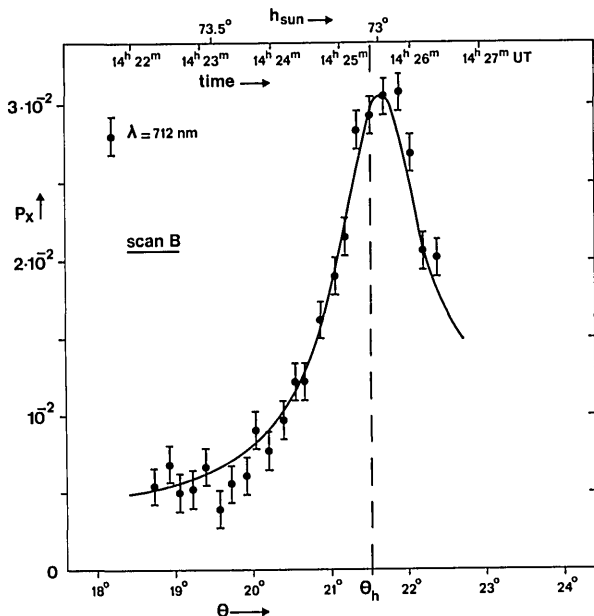


Fig. 12. Same as Fig. 8 but for the relatively short scan *B*. Data are shown for  $\lambda = 712$  nm. For  $\lambda = 441$  nm (not shown) the maximum in  $P_x$  was not encountered during this scan.

tion that both the halo scattering cross section at maximum halo intensity and the ratio  $I_B/I(18^\circ)$  are independent of wavelength,  $I_B(\lambda)$  can be calculated from

$$I_B(\lambda) = I_B(712)R(\lambda)Ir(\text{Sun}, 712)/Ir(\text{Sun}, \lambda), \quad (25)$$

where  $Ir(\text{Sun}, \lambda)$  is the solar intensity in a small bandwidth  $d\lambda$ .<sup>26</sup> The resulting values of  $I_B$  are consistent with the one derived from the photographic observation in Fig. 11 ( $I_B = 1.2$  at 590 nm) and are included in Table II.

The actual curve fitting of the  $Q$  points with the theoretical curve in Eq. (16) was done by solving the nonlinear regression interactively by successive linear

approximations,<sup>27</sup> where after each step the newly found value of  $\theta_h$  was substituted into Eq. (17) before the next iteration was started.

Table II gives the results of the regression. The last column gives the outcome of a  $\chi^2$  test of the observed points with the curve. The fact that the  $\chi^2$  values are comparable to the number of points involved indicates that the regression has been successful in the sense that the variance of the points with respect to the curve is neither larger nor smaller than what is to be expected from the standard deviations of the observed points. See also Figs. 8 and 12, where the solid lines are the regression lines.

The results of the  $\lambda = 542$ -nm channel have been omitted in Table II, since they were far less accurate than the others. The reason is the larger standard deviation in the observations (see Table I). For the same reason, the camera results have not been included. We note, however, that its results ( $A = 500 \pm 150 \times 10^{-4}$ ,  $\theta_h = 21.76 \pm 0.15^\circ$ , and  $\theta_{1/2} = 0.64 \pm 0.15^\circ$ ) are consistent with the MPF observations. For scan *B* we included only the results of the four longest wavelengths in Table II. The reason is that the scan stopped at  $\theta = 22.4^\circ$  and hence did not sufficiently pass the halo angle for the 402-481-nm wavelengths. For the longer wavelengths, this scan is still long enough to yield quite reliable values for the constants  $\theta_h$ ,  $\theta_{1/2}$ , and  $A$  of Eq. (16), although not for  $C$  and  $Q_B$ .

#### D. Interpretation of the La Palma Halo

##### Halo Identification

At high solar elevations, it is difficult to distinguish between the shape of a  $22^\circ$  halo and a circumscribed halo<sup>7</sup> caused, respectively, by random orientation and preferential orientation with the horizontally directed *C* axis. However, visual inspection during the La Palma halo indicated a poorly colored halo with a flat

Table II. Results of the Regression of Observed  $P_x$  Values with Eq. (16)<sup>a</sup>

Wavelength (nm)	$\theta_h$ (deg)	$\theta_{1/2}$ (deg)	$A \times 10^4$	$C \times 10^4$	$Q_B \times 10^4$	$U_B \times 10^4$	$I_B$	$\chi^2$
<b>Scan A</b>								
402	$22.61 \pm 0.03$	$0.36 \pm 0.05$	$474 \pm 38$	$174 \pm 33$	$-8 \pm 10$	$-113 \pm 7$	1.9	38
441	$22.44 \pm 0.03$	$0.54 \pm 0.03$	$418 \pm 18$	$145 \pm 24$	$-7 \pm 6$	$-59 \pm 3$	1.4	36
481	$22.32 \pm 0.03$	$0.61 \pm 0.04$	$377 \pm 15$	$120 \pm 20$	$16 \pm 5$	$-32 \pm 3$	1.2	25
622	$21.85 \pm 0.03$	$0.80 \pm 0.05$	$342 \pm 13$	$185 \pm 17$	$38 \pm 5$	$-15 \pm 2$	1.1	83
712	$21.66 \pm 0.04$	$0.89 \pm 0.06$	$295 \pm 11$	$222 \pm 13$	$40 \pm 9$	$-16 \pm 1$	1.0	39
791	$21.56 \pm 0.03$	$0.93 \pm 0.05$	$307 \pm 10$	$216 \pm 13$	$55 \pm 8$	$-13 \pm 2$	1.1	48
850	$21.38 \pm 0.08$	$1.09 \pm 0.12$	$366 \pm 25$	$329 \pm 33$	$4 \pm 24$	$5 \pm 4$	1.4	41
<b>Scan B</b>								
622	$21.83 \pm 0.06$	$0.59 \pm 0.06$	$407 \pm 63$	$213 \pm 118$	$12 \pm 9$	$-18 \pm 3$	1.1	33
712	$21.72 \pm 0.07$	$0.65 \pm 0.07$	$356 \pm 39$	$180 \pm 90$	$30 \pm 9$	$-14 \pm 2$	1.0	28
791	$21.61 \pm 0.05$	$0.69 \pm 0.06$	$348 \pm 37$	$201 \pm 60$	$25 \pm 8$	$-9 \pm 3$	1.1	30
850	$21.67 \pm 0.14$	$0.82 \pm 0.18$	$414 \pm 110$	$17 \pm 150$	$66 \pm 22$	$8 \pm 6$	1.4	20

<sup>a</sup> Equation (17) is used to transform  $P_x$  into the second Stokes parameter  $Q$ .  $A$  is the polarized intensity of the maximum height of the birefringence peak,  $C$  is the residual polarization, and  $Q_B$  and  $I_B$  are the background in  $Q$  and the background intensity, respectively.  $U_B$  is the background in the third Stokes parameter  $U$  obtained by averaging the  $P_y$  values. All the parameters,  $A$ ,  $C$ ,  $Q_B$ ,  $U_B$ , and  $I_B$ , are measured with respect to the maximum halo intensity ( $I_H$ )<sub>max</sub>.  $\theta_h$  is the halo angle and  $\theta_{1/2}$  is the angular separation between the maximum of the diffraction peak and its half-value point. The last column gives the results of a  $\chi^2$  test. The number of points is 38 for scan *A* and 23 for scan *B*.

intensity distribution. This favors the former identification.<sup>4,8</sup> This temporary conclusion can be confirmed with polarimetric measurements. For a scattering azimuth of  $204^\circ$  of a circumscribed halo and a solar elevation of  $70^\circ$ , the angle between the crystal  $C$  axis (which is the optical axis) and the Sun's rays is  $\sim 10^\circ$ . This skew incidence causes the circumscribed halo to be  $0.3^\circ$  further away from the Sun than the circular halo. Such a shift of halo angle is not found (see below). Furthermore, such a crystal configuration would cause a tilt of the direction of polarization of  $-1.9^\circ$  with respect to the scattering plane. This tilt occurs because the plane containing the optical axis of the crystal and the light ray determining the polarization does not cross the scattering plane at right angles, see also Ref. 28. Since in Figs. 8 and 9 we transformed the plane of reference of the Stokes vector to the scattering plane, this means that a maximum of  $P_x$  would be accompanied by a minimum of  $P_y$  if the halo is the circumscribed halo. The magnitude of the  $P_y$  peak would be  $\sin(2 \times 1.9^\circ)$  of that of the  $P_x$  peak and hence  $\sim 1.7 \times 10^{-3}$  in Fig. 9. We see no evidence of such a minimum and we conclude that the La Palma halo was indeed the result of randomly oriented crystals.

## V. Halo Angles

A comparison of Tables I and II shows that the observed halo angles are systematically higher than the calculated halo angles. For scan A the mean difference is  $0.12 \pm 0.012^\circ$ ; for scan B it is  $0.17 \pm 0.03^\circ$ . If the  $0.02^\circ$  pointing uncertainty of the telescope is taken into account, the standard deviation of these numbers changes to  $0.02^\circ$  and  $0.04^\circ$ , respectively. However, the numbers in Table I were calculated with an index of refraction with respect to vacuum and for a temperature of  $-3^\circ\text{C}$ .<sup>23</sup> We denote this halo angle by  $\theta_h(-3^\circ\text{C})$ . Then, for a pressure level of 22.5 kPa and a temperature  $T$  in degrees Celsius, from the temperature dependence of the index of refraction,<sup>23</sup> the index of refraction of air,<sup>26</sup> and the well-known minimum deviation formula for the  $22^\circ$  halo, we find that

$$\theta_h(T) - \theta_h(-3^\circ\text{C}) = -76^\circ (20 + 3.82T) \times 10^{-5}. \quad (26)$$

The observed differences in the halo angle yield, with Eq. (26), a crystal temperature of  $T = -48 \pm 7^\circ\text{C}$  for scan A and  $T = -64 \pm 14^\circ\text{C}$  for scan B, in agreement with the cloud temperature of  $-54^\circ\text{C}$ , as observed by the Tenerife vertical sounding. The uncertainty of  $7^\circ\text{C}$  in the scan A crystal temperature is caused chiefly by the uncertainty of  $0.02^\circ$  in the pointing of the telescope. Hence the agreement with cloud temperature means that the polarimetrically observed halo angles agree to within this pointing uncertainty of  $0.02^\circ$  with the theoretical halo angles. Figure 13 shows a plot of  $\theta_h(\text{observed}) - \theta_h(-3^\circ\text{C})$  as a function of wavelength. We note that, for the high solar elevation and the high elevation of the scan, the effect of atmospheric refraction on the observed halo angle can be neglected since it amounts to only  $3 \times 10^{-3}$  deg.

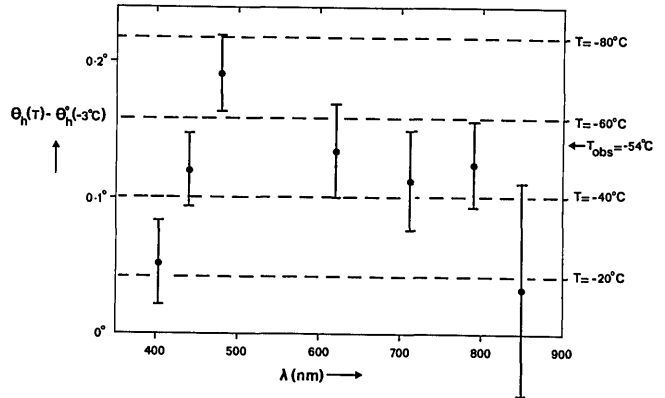


Fig. 13. Observed halo angles minus those calculated for an index of refraction with respect to vacuum and a temperature of  $-3^\circ\text{C}$ . The latter is denoted by  $\theta_h(-3^\circ\text{C})$ . The dashed lines indicate the halo angles for different crystal temperatures and an atmospheric pressure of 22.5 kPa,  $\theta_h(T)$ , relative to  $\theta_h(-3^\circ\text{C})$ . The observed air temperature at the level of the crystals was  $-54^\circ\text{C}$ , as measured by the vertical sounding from Tenerife.

## VI. Crystal Size

Parameter  $\theta_{1/2}$  in Table II allows the calculation of the effective slit width of the crystals. Figure 14 shows a plot of  $\theta_{1/2}$  as a function of wavelength for scan A. The observed values have been corrected for the smearing by the solar disk by using Eq. (14). Hence, the presented values of  $\theta_{1/2}$  can be attributed to diffraction alone.

Figure 14 also includes a least-squares regression line through the observations. As expected from Eq. (12), it passes close to the origin and thus Eq. (12) can be used to determine  $a_{\text{eff}}$ . The resulting values are  $a_{\text{eff}} = 15.4 \pm 0.04 \mu\text{m}$  for scan A and  $a_{\text{eff}} = 20.5 \pm 1.2 \mu\text{m}$  for scan B. Then diameters  $d$  of the hexagon-shaped face of the crystals are found from Eq. (23) and result in scan A:  $d = 41 \pm 1.1 \mu\text{m}$ , scan B:  $d = 54 \pm 3.0 \mu\text{m}$ . Scan A took place much closer to the edge of the cloud; the difference between these sizes may be attributed to the inhomogeneities within the crystal cloud.

## VII. Amplitude of the Birefringence Peak

The significance of polarimetry for halo detection depends strongly on ratio  $A$  of the amplitude of the sharp birefringence peak in  $Q(\theta)$  and the maximum intensity of the halo. As mentioned above, for the solar-disk-smeared  $22^\circ$  halo,  $A$  ranges between 0.15 and 0.02, being a function of broadening of the birefringence peak,  $\theta_{1/2}$ .

Figure 15 compares the measured values of  $A$  with the theory, relation (20) and Eq. (18). To suppress noise in the  $\theta_{1/2}$  values, they are not taken directly from Table II but are recalculated from the  $a_{\text{eff}}$  values determined above. The theoretical line has been calculated assuming  $\alpha = 0.4 \text{ deg}^{-1}$  in Eq. (18). Adopting  $\alpha = 0.3 \text{ deg}^{-1}$  results in a lowering of the  $A$  values by only 0.003.

Figure 15 indicates that the agreement is good in spite of the fact that  $A$  in each scan may contain a systematic relative error of  $\sim 15\%$ . We emphasize that the curve in Fig. 15 is valid exclusively for the circular

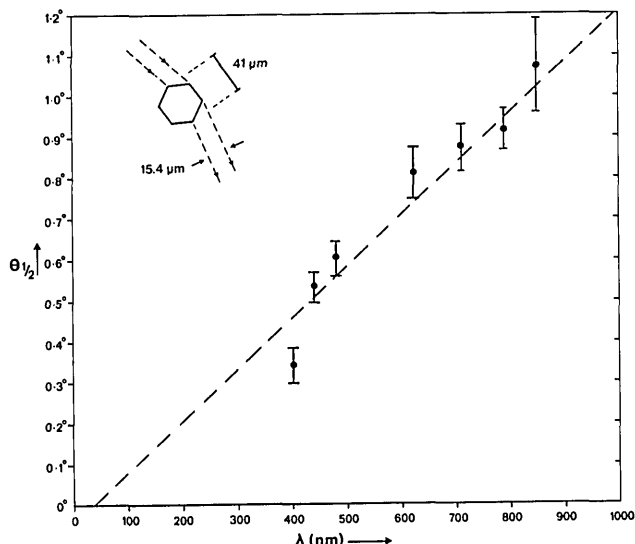


Fig. 14. Diffraction broadening of the birefringence peak as a function of wavelength for scan A. The observed values have been corrected for broadening by the solar disk. The dashed line is a regression line with the observations. Its slope indicates an effective slit width of the crystal of  $15.4 \pm 0.04 \mu\text{m}$  and hence a crystal diameter of  $41 \pm 1.1 \mu\text{m}$ .

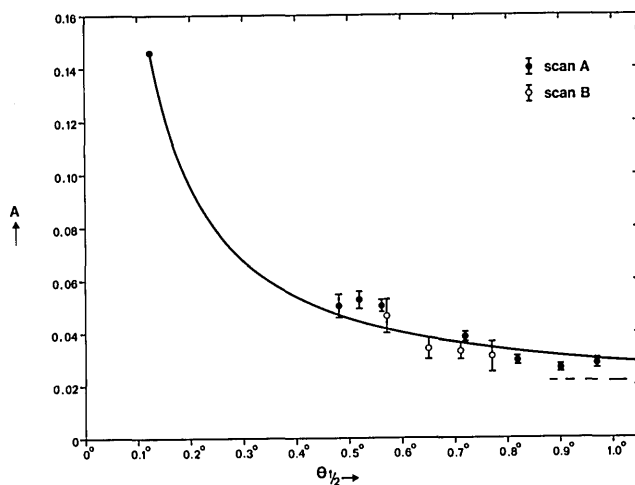


Fig. 15. Amplitude  $A$  of the sharp birefringence peak of the  $22^\circ$  halo in  $Q$  relative to the maximum halo intensity as a function of the broadening of the peak,  $\theta_{1/2}$ . The solid curve is the theoretical curve. Its asymptotic value is indicated by a dashed line. The point at  $\theta_{1/2} = 0.12^\circ$  indicates the situation where the diffraction broadening is small with respect to the width of the solar disk.

$22^\circ$  halo; other halos (parhelia,  $46^\circ$  halos, etc.) may result in larger values if either  $\Delta\theta_h$  or  $\alpha$  is larger.

### VIII. Residual Polarization and Intrinsic Polarization

Only scan A provided reliable values for the residual polarization of halo C. Its mean value from Table II is  $0.020 \pm 0.001$ , which modifies to  $0.020 \pm 0.004$  if the estimated uncertainty in  $I_B$  and the relatively large scatter in the set of observed values are taken into account. This is still significantly smaller than the value of  $0.087$  expected in the absence of birefringence.

With Eq. (21), this discrepancy of  $0.017 \pm 0.004$  leads to a value of  $3.2 \pm 0.8 \text{ deg}^{-1}$  for  $\alpha = -I'_g(\theta)/I_g(\theta)$ . Within the uncertainty, this is in agreement with the simulation given in Fig. 2 and is also consistent with the observations of Lynch and Schwartz,<sup>14</sup> leading to  $\alpha = 4.3 \text{ deg}^{-1}$  for  $\theta > 24^\circ$ .

The maximum intrinsic halo polarization  $(P_H)_{\max}$  can be calculated from the data in Table II using relation (22). No significant wavelength dependence is present in it. Averaged over all observations of scan A,  $(P_H)_{\max} = 0.087 \pm 0.002$ .

Normally, a degree of polarization of the order of 0.1 is not visible by visual inspection with a polarizer, but halo polarization is an exception because rotation of the polarizer causes a shift of the halo rather than a variation of intensity. Therefore, our sensitivity for detecting halo polarization depends on our capability to locate the halo inner-edge position in the sky. The Mach–Seeliger perception theory, which has also been proved to apply to halo edges,<sup>29</sup> indicates that this capability is surprisingly good. This situation is improved by the color of the halo, which discriminates halo light from the background. This accounts, e.g., for the small standard deviation in visual halo radius observations, even if these are obtained on different days.<sup>30</sup> In the case of visual polarization observation, the situation is even more favorable, because the halo intensity is obviously constant during the observation and the cloud structures near the halo can be used as a reference. These facts explain the good visibility of halo shift in polarized light. As the magnitude of the shift is related to the amplitude of the birefringence peak, the governing factor of the visibility of halo polarization is the intrinsic polarization  $2A$  of this peak rather than the total intrinsic halo polarization itself.

### IX. Background Polarization

The Stokes parameters of background polarization, expressed in degree of polarization, can be found from Table II by using  $P_x = Q_B/I_B$  and  $P_y = U_B/I_B$ . The results, to which the correction for the zero-point polarization (Table I) has been applied, are given in

Table III. Polarization of the Background Intensity on Which the Halo Signal Is Superposed<sup>a</sup>

Wavelength (nm)	$P_x \times 10^4$	$P_y \times 10^4$	$P_{sc} \times 10^4$	$P_{vert} \times 10^4$
402	$-27 \pm 7$	$-56 \pm 6$	$-142 \pm 19$	$127 \pm 14$
441	$-28 \pm 8$	$-48 \pm 6$	$-126 \pm 20$	$109 \pm 14$
481	$-13 \pm 7$	$-40 \pm 7$	$-95 \pm 21$	$91 \pm 14$
622	$29 \pm 7$	$-22 \pm 4$	$-16 \pm 15$	$50 \pm 8$
712	$47 \pm 7$	$-16 \pm 3$	$14 \pm 13$	$36 \pm 6$
791	$53 \pm 7$	$-14 \pm 4$	$24 \pm 15$	$32 \pm 8$
850	$3 \pm 17$	$15 \pm 6$	$37 \pm 29$	$-34 \pm 12$

<sup>a</sup> The Stokes parameters are expressed in degree of polarization.  $P_x$  and  $P_y$  are the second and third Stokes parameters divided by the intensity; the plane of reference is the scattering plane. In the last column, the polarization has been decomposed on a nonorthogonal basis consisting of the scattering plane and the celestial vertical. The resulting parameters are  $P_{sc}$  and  $P_{vert}$ . This decomposition separates one particular type of multiple scattering from the others (see text).

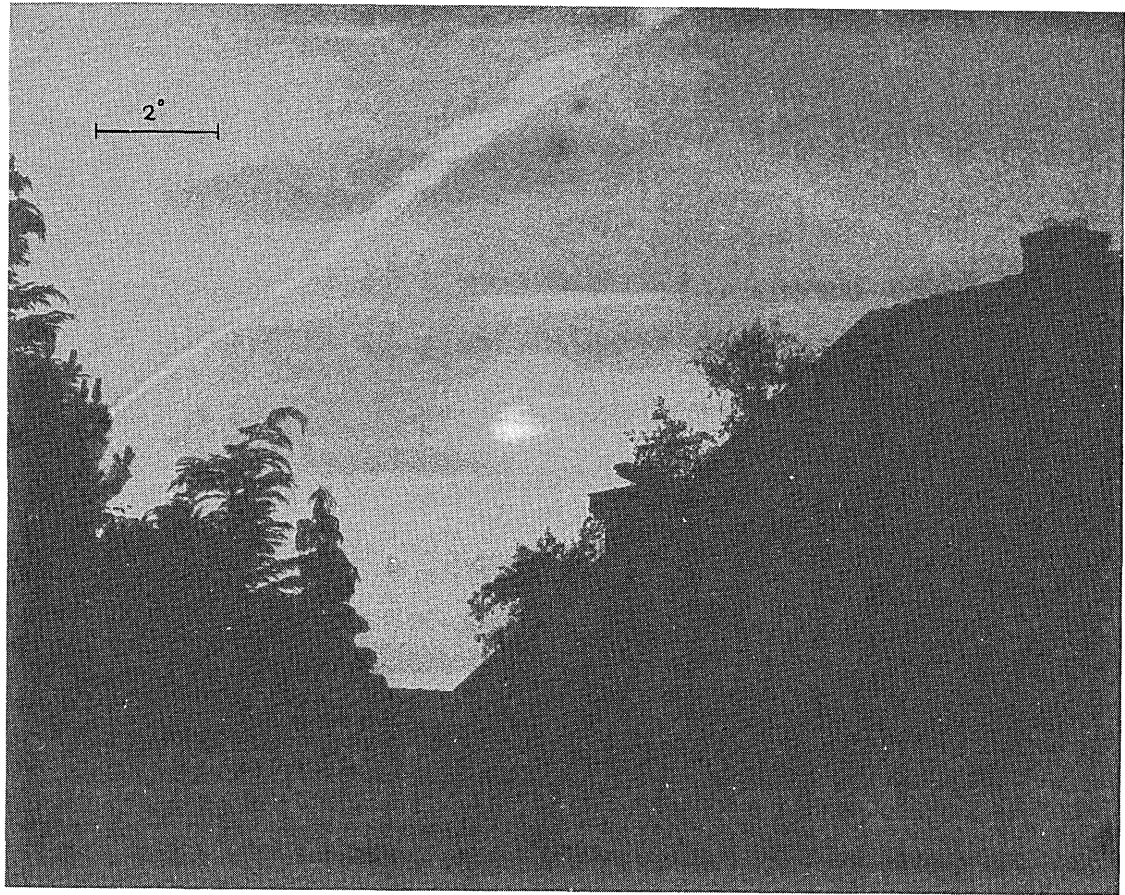


Fig. 16. Bright parhelion photographed with the polarimetric camera on 13 June 1988 at a solar elevation of 8.5°.

Table III. Also included in Table III is a decomposition of  $(P_x, P_y)$  into  $P_{sc}$  and  $P_{vert}$ . Here  $P_{sc}$  has the plane of scattering as a reference and  $P_{vert}$  has the celestial vertical.  $P_{sc}$  and  $P_{vert}$  are not orthogonal since the scattering plane is tilted by  $13^\circ$  with respect to the vertical (Fig. 6). The advantage of this decomposition is that it isolates a particular case of multiple scattering, i.e., the one where the last scattering center is located below the layer of large optical thickness. In this contribution, the incident light is the skylight and hence the symmetry axis of the scattering is the zenith. If the sky is brightest near the horizon, the polarization that occurs at the last scattering center  $P_{vert}$  is positive, otherwise it is negative.<sup>31</sup> Table III indicates that mainly the former situation materialized. This is to be expected if the cloud is still rather transparent. The fact that  $P_{vert}$  decreases the wavelength may be attributed to a lower luminosity near the horizon because of the smaller Rayleigh scattering cross section.

The other component,  $P_{sc}$ , is partly caused by multiple scattering in the cloud. Another part might be caused by single scattering by halo-generating crystals. However, our Monte Carlo simulation showed that this contribution is only 300 in the units of Fig. 2 and thus at least 1 order of magnitude less than the intensity of the halo maximum. Since the observed background intensity is of the order of the halo intensity, it must be caused by multiple scattering in the cloud and/or per-

haps by single scattering by particles other than halo-generating crystals. Hence, no further information about the physical state of these crystals is obtainable from the background polarization.

#### X. Intensity Slope versus Birefringence Peak Width

Within the present formalism the  $\theta_{1/2}$  value obtained from polarimetry is directly linked to the maximum slope of the halo intensity distribution, Eq. (24). This can be tested with the current set of data. The MPF intensity scan in Fig. 10 is not suitable for this, since the fluctuation in it prevents an accurate estimate of the slope, but the photographic record of the intensity in Fig. 11 is smooth enough for this purpose. Figure 11 yields  $(I_H')_{\max}/(I_H)_{\max} = 0.45 \pm 0.03 \text{ deg}^{-1}$ , which corresponds to  $\theta_{1/2} = 0.71 \pm 0.05^\circ$  [Eq. (24)]. With Eq. (12) and  $\lambda = 590 \text{ nm}$  this gives a slit width of  $15.4 \pm 1.0 \mu\text{m}$ . The agreement of this value with the one derived from polarimetry is perfect.

#### XI. Parhelion

On 13 June 1988 at 18:46 UT, we recorded a bright parhelion with the polarimetric camera. The place of observation was  $52.19^\circ\text{N}$  and  $5.28^\circ\text{E}$ , the solar elevation was  $8.5^\circ$ . Figure 16 shows the picture, Figs. 17 and 18 show the intensity and  $P_x$ , respectively, of the parhelion, scanned straight through the intensity maximum of the halo. The plane of reference of the Stokes

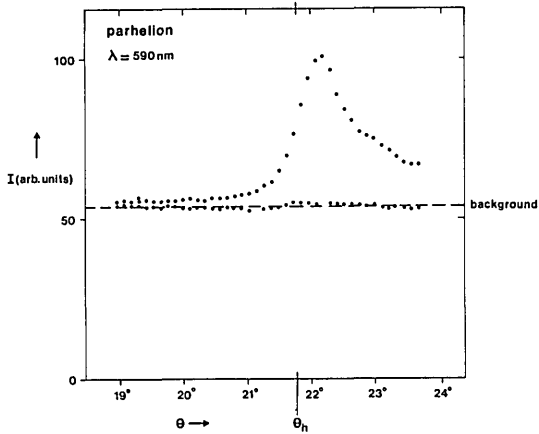


Fig. 17. Intensity of the parhelion in Fig. 16 as a function of scattering angle  $\theta$ , scanned through the halo intensity maximum. The background level is taken from a scan  $1.4^\circ$  below the parhelion. The absolute value of the scattering angle is not known: here we assumed that the polarization maximum (Fig. 18) coincides with the halo angle  $\theta_h$ .

parameter is the horizontal rather than the scattering plane, but for this low solar elevation the angle between these planes is  $<2^\circ$ .  $P_y$  did not show significant fluctuations and is not shown. We were unable to get the Sun in the Sun finder of the camera when the picture was taken, so that the absolute value for the scattering angle is not known. In Figs. 17 and 18 we have assumed that the peak in the polarization coincides with the halo angle.

It is instructive to compare the parhelion observation with the La Palma halo. Figure 17 shows a more pronounced halo intensity peak and Fig. 18 indicates a stronger polarization in a narrower angular range. One reason for this is a larger crystal size, but part of the effect may result from the fact that the parhelion light distribution differs essentially from that of the  $22^\circ$  halo.<sup>4,7,28</sup> In fact, for an exact interpretation of the parhelion, the present model with Eq. (16) should be carefully reevaluated and perhaps slightly modified, but for a single observation, this seems overdone. Qualitative conclusions can already be drawn from the present model because for a parhelion the polarization also results from a broadened birefringence peak.

The conclusions are the following. The slope of the intensity distribution near  $\theta_h$  is much larger than that of the La Palma halo. The value of  $(I_H')_{\max}/(I_H)_{\max}$  is  $1.8 \pm 0.1 \text{ deg}^{-1}$ , corresponding to  $\theta_{1/2} = 0.18 \pm 0.01^\circ$ . This is only  $0.06^\circ$  larger than the broadening caused by the solar disk. With Eqs. (12) and (14), this indicates a slit width of  $83 \pm 6 \mu\text{m}$  and hence a crystal diameter of  $d = 220 \pm 17 \mu\text{m}$ . The polarimetric scan gives  $\theta_{1/2} \approx 0.23^\circ$ , but the shape of the  $P_x$  scan resembles a solar disk-broadened peak more closely than a diffraction-broadened peak. Fitting with the latter to obtain  $\theta_{1/2}$  proved to be less accurate; its results provide only a lower limit to the crystal size, of the order of  $150 \mu\text{m}$ .

The degree of polarization is very large; the intrinsic polarization in the birefringence peak rises to 40% and

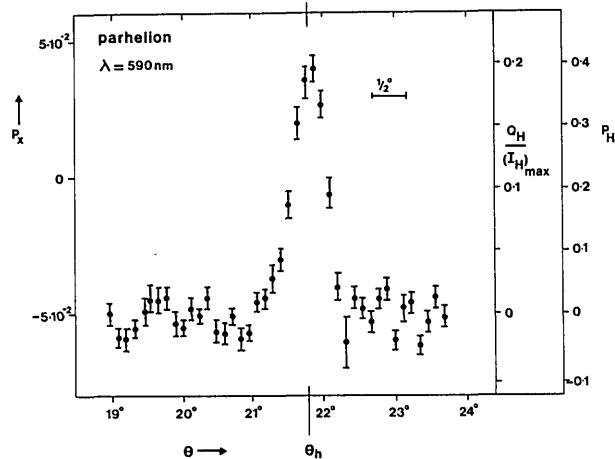


Fig. 18. Second Stokes parameter  $P_x$  expressed in degree of polarization for the parhelion in Fig. 16. Two alternative ordinates are indicated on the right.  $Q_H$  and  $(I_H)_{\max}$  are the second Stokes parameter and the maximum intensity, respectively, of the parhelion; the maximum of  $Q_H/(I_H)_{\max}$  corresponds to parameter  $A$ . The extreme right axis gives an indication of the intrinsic halo polarization  $P_H$ . The absolute value of scattering angle  $\theta$  is not known; we have assumed that the polarization maximum coincides with the halo angle  $\theta_h$ . Note that the polarization of the parhelion is stronger than that of the La Palma halo and that the peak is narrower.

$A = 0.2$ . This is five times larger than the La Palma value and exceeds even the limiting value in Fig. 15. However, the limiting value for a parhelion may be different from that for a  $22^\circ$  halo since the intensity distribution is different. A previous analysis of this type of distribution gave  $A = 0.21$  if the crystals are large (Ref. 4, Fig. 8), and that number fits the observation.

## XII. Discussion and Conclusions

Little quantitative information is available in the literature about the properties of light distributions of natural halos. Polarimetric observations have been published in one case<sup>32</sup> but never for refraction halos. So we are left with intensity distributions with which to compare our results but only two observations of that type have been reported. The first is by Brüche and Brüche,<sup>29</sup> the other is by Lynch and Schwartz.<sup>14</sup> Both are densitometer scans of pictures of the  $22^\circ$  halo, and both pictures were taken without the use of a color filter. Still, the measurements are detailed enough to determine with some accuracy the effective crystal diameter from the maximum slope of the intensity distribution, particularly for the latter observation. Using Eqs. (12), (23), and (24) and adopting  $\lambda = 500 \text{ nm}$ , we obtain  $d = 55 \pm 5 \mu\text{m}$  for the Brüche and Brüche halo and  $d = 44 \pm 3 \mu\text{m}$  for the Lynch and Schwartz halo. The quoted errors in these estimates only allow for the uncertainty in the slope determination. The values of the crystal size are consistent with our La Palma observations. This agreement supports the view that halo formation by randomly oriented crystals places the crystal size between stringent boundaries.<sup>8,33</sup> However, compared to the prediction of the

Fraser<sup>8</sup> model of crystal disorientation by Brownian motion, the crystal diameters are rather large. A possible reason can be a bias in our method of crystal size determination caused by the adoption of a certain type of size distribution. However, Tape<sup>34</sup> collected crystals during a nearby 22° halo display and his Fig. 3 indicates diameters of the crystal hexagons of the same order as ours.

Our parhelion observations indicate a much larger crystal diameter than those causing the La Palma halo. The 220-μm size is in good agreement with the light pillar crystals measured by Sassen<sup>33</sup> but are considerably larger than the parhelion crystals collected by Tape.<sup>34</sup> Apparently, there is a relatively large degree of freedom in the crystal size responsible for parhelia<sup>8,33</sup> and hence the diffraction broadening may differ from case to case. Our large crystal parhelion was exceptionally bright with a sharp and vividly colored inner edge, by no means a typical parhelion.

From the foregoing we might conclude that crystal size determination from the light or polarization distribution of halos is quite possible, provided that the crystals are small enough to provide diffraction broadening. Particularly for the 22° halos, the agreement between the optical determination of crystal sizes and the sampling data is encouraging. Still this agreement is of a qualitative nature since the observations took place on different occasions. Polarimetry and photometry of nearby halos with simultaneous crystal sampling are required to enhance the understanding of the relation between crystal sizes and halos.

As a straightforward result, our measurements confirm the existence of strong halo polarization in a narrow scattering angular range. This shows that, in the case of birefringence, halo polarimetry is a much more sensitive method for detecting crystals in the terrestrial atmosphere or in the atmospheres of other planets or their satellites than was previously anticipated.<sup>11</sup> The sharp halo birefringence peak in the polarization provides a sensitive diagnostic and the stability of the degree of polarization in fluctuating crystal densities, indicated by the current measurements, improves its detectability. Since the magnitude of the peak is inversely proportional to its width, the method is more sensitive for large crystals. In general, to resolve the peak, polarimetric observations of high angular resolution are required. The peak is centered at the halo angle and, once resolved, halo angles can be determined with high accuracy, as demonstrated by the La Palma measurements.

Up to now, calculation of halo angles of crystals that may occur in planetary atmospheres has been restricted to the cubic class,<sup>35,36</sup> but a few anisotropic candidates have also been suggested.<sup>35</sup> These include ice, nitrogen, the ammonia hydrates, and sulfur dioxide, and there may be more. However, as refraction halos of significant intensity always appear at a scattering angle much smaller than 90°, a hypothetical halo in a planetary atmosphere is only visible at the far side of the planet. Thus for an earth-bound observer, only the inner planets can be examined for halos. This was

the aim of our La Palma campaign, where we did obtain the required data<sup>5,6</sup> for Venus and which yielded this paper as a fortunate by-product. For the outer planets, halo scattering can never reach the earth. Therefore, a search for birefringent crystals in the often complicated atmospheres of the outer planets must wait until a future fly-by, orbiting, or landing spacecraft carries a high-resolution polarimeter.

#### Appendix A: Diffraction Broadening of an Exponential Halo Intensity Distribution

We consider a geometric halo intensity function for  $\theta > \theta_h$  of the form

$$I_g(\theta) = (I_g)_{\max} \exp[-\alpha(\theta - \theta_h)], \quad (A1)$$

where  $(I_g)_{\max} = I_g(\theta_h) = 1$ . The halo intensity distribution after convolution with diffraction function  $g$  [Eq. (11)] is denoted by  $I_H(\theta)$ .  $(I_g)_{\max}/(I_H)_{\max}$  is given by Eq. (18) and with  $(I_g)_{\max} = 1$  can be approximated by

$$1/(I_H)_{\max} = 1 + \frac{1}{2}\pi\alpha\theta_{1/2} + \frac{1}{12}(\pi\alpha\theta_{1/2})^2 - \frac{1}{720}(\pi\alpha\theta_{1/2})^4 + \dots \quad (A2)$$

For  $I_H(\theta)$  one finds that

$$I_H(\theta_h) \approx \frac{1}{2} - \frac{\alpha\theta_{1/2}}{\pi}, \quad (A3)$$

$$I_H'(\theta_h) = \frac{1}{\pi\theta_{1/2}} - \alpha I_H(\theta_h), \quad (A4)$$

$$I_H''(\theta_h) = -\alpha I_H'(\theta_h), \quad (A5)$$

$$I_H'''(\theta_h) = -\frac{2}{\pi\theta_{1/2}^3} - \alpha I_H''(\theta_h). \quad (A6)$$

The inflection point of  $I_H(\theta)$  can be found in first approximation from Eqs. (A5) and (A6), which gives  $\theta_{\text{infl}} - \theta_h = -I_H''(\theta_h)/I_H'''(\theta_h) \approx -\frac{1}{2}\alpha\theta_{1/2}^2$ . Then,  $(I_H')_{\max} \approx I_H'(\theta_h) - \frac{1}{2}\alpha\theta_{1/2}^2 I_H''(\theta_h)$ . Combining this with Eq. (A2) leads to

$$(I_H')_{\max}/(I_H)_{\max} = \frac{1}{\pi\theta_{1/2}}. \quad (A7)$$

The next term in Eq. (A7) is  $-0.1\pi\alpha^2\theta_{1/2}$ . Hence, the relative truncation error in Eq. (A7) is of the order of  $(\alpha\theta_{1/2})^2$ .

We thank R. S. Le Poole for assistance in using the Leiden Astroscan densitometer, H. Deen for adaptation of the polarimetric camera, R. E. Wallis for his support during the measurements, S. Kruizinga and T. A. Buishand for statistical advice, G. D. Kelderman for software advice, and A. P. M. Baede for general encouragement. G. P. Können thanks W. Tape for his comments on the draft of this paper during our cool stay at the South Pole.

The Jacobus Kapteyn telescope is operated on the island of La Palma by the Royal Greenwich Observatory in the Spanish Observatorio del Roque de los Muchachos of the Instituto de Astrofísica de Canarias.

This work was financially supported by the Leids Kerkhove Bosscha Fonds, the Leids Sterrenwacht Fonds, and by The Netherlands Organization for Scientific Research.

## References

1. T. Gehrels, eds., *Planets, Stars and Nebulae, Studied with Photopolarimetry* (U. Arizona Press, Tucson, Ariz., 1974).
2. J. E. Hanssen and J. W. Hovenier, "Interpretation of the polarization of Venus," *J. Atmos. Sci.* **31**, 1137–1160 (1974).
3. G. P. Können, "Polarisation of haloes and double refraction," *Weather* **32**, 467–468 (1977).
4. G. P. Können, "Polarization and intensity distributions of refraction halos," *J. Opt. Soc. Am.* **73**, 1629–1640 (1983).
5. G. P. Können and J. Tinbergen, "Venus crystals and halo scattering," in *Technical Digest on Light and Color in the Open Air*, Vol. 12 of OSA 1990 Technical Digest Series (Optical Society of America, Washington, D.C., 1990), pp. 78–79.
6. G. P. Können, A. A. Schoenmaker, and J. Tinbergen, "Polarimetric search for ice crystals in the upper atmosphere of Venus," to be submitted to *Icarus*.
7. R. Greenler, *Rainbows, Halos and Glories* (Cambridge U. Press, Cambridge, England, 1980).
8. A. B. Fraser, "What size of ice crystals causes the halos?," *J. Opt. Soc. Am.* **69**, 1112–1118 (1979).
9. P. Drude, "Doppelbrechung," in *Handbuch der Physik*, A. Winckelmann, ed. (Joh. Barth, Leipzig, 1906), Vol. 6.
10. S. Szyvessy, "Kristaloptik," in *Handbuch der Physik*, H. Konen, Ed. (Springer, Berlin, 1928), Vol. 20.
11. B. T. O'Leary, "The presence of ice in the Venus atmosphere as inferred from a halo effect," *Astrophys. J.* **146**, 754–766 (1966).
12. F. Pattloch and E. Tränkle, "Monte Carlo simulation and analysis of halo phenomena," *J. Opt. Soc. Am. A* **1**, 520–526 (1984).
13. W. Tape, Department of Mathematical Sciences, University of Alaska at Fairbanks, Fairbanks, Alaska 99775-1110 *Halos: Celestial Manifestations of Crystalline Beauty* (personal communication of book in preparation).
14. D. K. Lynch and P. Schwartz, "Intensity profile of the 22° halo," *J. Opt. Soc. Am. A* **2**, 585–589 (1985).
15. C. F. Bohren and D. F. Huffman, *Absorption and Scattering of Light by Small particles* (Wiley Interscience, New York, 1983).
16. H. C. van de Hulst, *Multiple Light Scattering* (Academic, New York, 1980), Vol. 2.
17. H. R. Pruppacher and J. D. Klett, *Microphysics of Clouds and Precipitation* (Nijhoff, Dordrecht, The Netherlands, 1978).
18. J. Tinbergen, in *Observers' Guide for the Isaac Newton Group of Telescopes, La Palma* (Royal Greenwich Observatory, Cambridge, 1988).
19. G. P. Können and J. Tinbergen, "Venus, meteorology and the Jacobus Kapteyn telescope," *Gemini* **22**, 12–13 (Dec. 1988).
20. J.-C. Hsu and M. Breger, "On standard polarized stars," *Astrophys. J.* **262**, 732–738 (1982).
21. P. A. Bastiaansen, Leiden Observatory, P.O. Box 9513, 2300RA Leiden, The Netherlands (personal communication, 1984).
22. J. Tinbergen, "A list of zero polarization standards," *Astron. Astrophys. Suppl. Ser.* **35**, 325–326 (1979).
23. P. V. Hobbs, *Ice Physics* (Clarendon, Oxford, 1974), p. 202.
24. R. L. Kurucz, "Model atmospheres for G, F, A, B and O stars," *Astrophys. J. Suppl. Ser.* **40**, 1–130 (1979).
25. H. Tüg, N. M. White, and G. W. Lockwood, "Absolute energy distributions of  $\alpha$  Lyrae and 109 Virginis from 3295 Å to 9040 Å," *Astron. Astrophys.* **61**, 679–684 (1977).
26. R. C. Weast, ed., *Handbook of Chemistry and Physics* (CRC Press, Cleveland, Ohio, 1972).
27. T. M. Wonnacott and R. J. Wonnacott, *Regression: a Second Course in Statistics* (Wiley, New York, 1981).
28. W. Tape, "Geometry of halo formation," *J. Opt. Soc. A* **69**, 1122–1132 (1979).
29. E. Brüche and D. Brüche, "Über die Photometrie von Sonnenringen," *Meteorol. Z.* **49**, 289–294 (1939).
30. J. M. Perner and F. M. Exner, *Meteorologische Optik* (Wilhelm Braumüller, Wien, 1910), pp. 229–230.
31. G. P. Können, *Polarized Light in Nature* (Cambridge U. Press, Cambridge, England, 1985).
32. K. Sassen, "Polarization and Brewster angle properties of light pillars," *J. Opt. Soc. Am. A* **4**, 570–580 (1987).
33. K. Sassen, "Remote sensing of planar ice crystal fall attitudes," *J. Meteorol. Soc. Jpn.* **58**, 422–429 (1980).
34. W. Tape, "Some ice crystals that made halos," *J. Opt. Soc. Am.* **73**, 1641–1645 (1983).
35. E. Whalley and G. E. McLaurin, "Refraction halos in the solar system I. Halos from cubic crystals that may occur in the solar system," *J. Opt. Soc. Am. A* **1**, 1166–1170 (1984).
36. P. Doherty and C. Bennett, "Carbon dioxide ice halos on Mars: a prediction from crystal growth experiments," in *Technical Digest of Topical Meeting on Meteorological Optics*, Vol. 8 of OSA 1986 Technical Digest Series (Optical Society of America, Washington, D.C., 1986), pp. 20–23.